JGR Solid Earth

RESEARCH ARTICLE
10.1029/2021JB022202

Shear Velocity Inversion Guided by Resistivity Structure From the PI-LAB Experiment for Integrated Estimates of Partial Melt in the Mantle

Nicholas Harmon[1], Shunguo Wang[2], Catherine A. Rychert[1], Steven Constable[3], and J. Michael Kendall[4]

[1]School of Ocean and Earth Science, University of Southampton, Southampton, UK, [2]Department of Electronic Systems, Norwegian University of Science and Technology, Trondheim, Norway, [3]Scripps Institution of Oceanography, University of California San Diego, San Diego, CA, USA, [4]Department of Earth Science, Oxford University, Oxford, UK

Key Points:

- Shear-wave velocities from surface waves correlate with resistivity at the equatorial Mid-Atlantic Ridge and agree with petrophysics models
- Using a starting velocity model derived from a petrophysical relationship increases agreement between velocity and resistivity
- Velocity and resistivity provide good constraints on Earth properties and suggest up to 4% melt with high-volatile content

Correspondence to:
N. Harmon,
N.Harmon@noc.soton.ac.uk

Citation:
Harmon, N., Wang, S., Rychert, C. A., Constable, S., & Kendall, J. M. (2021). Shear velocity inversion guided by resistivity structure from the PI-LAB experiment for integrated estimates of partial melt in the mantle. *Journal of Geophysical Research: Solid Earth*, *126*, e2021JB022202. https://doi.org/10.1029/2021JB022202

Received 8 APR 2021
Accepted 7 AUG 2021

Abstract

The lithosphere-asthenosphere system is fundamental to our understanding of mantle convection and plate tectonics. The different sensitivities of seismic and electromagnetic methods can be used together to better constrain the properties of the system. Here, we re-examine the shear velocity model from Rayleigh waves in light of the magnetotelluric based resistivity models from the Passive Imaging of the Lithosphere Asthenosphere Boundary (PI-LAB) experiment near the equatorial Mid-Atlantic Ridge, with the goal of generating a structurally consistent velocity and resistivity model for the region. Cross-plots of the models suggest a linear or near-linear trend that is also in agreement with petrophysical predictions. We generate a new shear velocity model from the resistivity models based on petrophysical relationships. The new velocity model fits the phase velocity data, and the correlation coefficient between the shear velocity and resistivity models is increased. Much of the model can be predicted by expectations for a thermal half-space cooling model, although some regions require a combination of higher temperatures, volatiles, or partial melt. We use the petrophysical predictions to estimate the melt fraction, melt volatile content, and temperature structure of the asthenospheric anomalies. We find up to 4% melt, with the lowest resistivities and shear velocities explained by up to 20% water or 20% CO_2 in the melt or ~1% nearly pure sulfide melt, depending on the set of assumptions used. Melt is required in punctuated anomalies over broad depth ranges, and also in channels at the base of the lithosphere. Melt in the asthenosphere is dynamic, yet persistent on geologic timescales.

Plain Language Summary

Constraints on the tectonic plate and its relationship to the deeper mantle are important for a better understanding of the planet. Seismic and electromagnetic methods are our primary means of determining its structure and physical properties. They also offer different sensitivities to Earth's properties. We plot seismic velocity versus resistivity near the equatorial Mid-Atlantic Ridge. A linear or near-linear trend is suggested in agreement with laboratory predictions. We map the resistivity model to a new shear-wave starting model using the petrophysical relationship, and re-invert for shear-wave velocity. The resulting shear-wave velocity model agrees with the original data and correlates better with the resistivity models. Much of the result can be predicted by temperature, but not everywhere. We estimate the temperature, melt fraction, and melt volatile content of the asthenospheric anomalies and find up to 0.04 melt fraction with relatively high-volatile contents. Melt is required in punctuated anomalies over broad depth ranges and also in channels at the base of the lithosphere. Melt in the asthenosphere is dynamic, yet persistent on geologic timescales.

1. Introduction

Plate tectonic theory is predicated on the idea of a rigid lithosphere that overrides a weaker underlying asthenosphere (McKenzie & Parker, 1967), but the nature of the lithosphere-asthenosphere system remains the subject of vigorous debate. The oceanic lithosphere comprises the majority of the surface of the Earth and has the simplest evolution and history. It is classically thought to be thermally defined as a boundary layer in a simple thermal model (Parker & Oldenburg, 1973). In this model, increasing temperature with depth causes mantle rocks to weaken, creating the asthenosphere (e.g., Goetze et al., 1978). However, a host of observations, including sharp seismic velocity discontinuities (Fischer et al., 2020; Gaherty et al., 1996;

Kawakatsu et al., 2009; Rychert & Harmon, 2018; Rychert, Harmon & Tharimena, 2018a, 2018b; Rychert & Shearer, 2011; Rychert et al., 2020; Schmerr, 2012; Tan & Helmberger, 2007; Tharimena et al., 2017), low-velocity zones (Forsyth et al., 1998; Harmon et al., 2020), and low resistivity zones (Baba et al., 2006; Johansen et al., 2019; Key et al., 2013; Naif et al., 2013; Wang et al., 2020) in the asthenosphere, suggest that in addition to temperature other factors are likely required to explain the observations. Many potential explanations of these observations have been proposed including for instance an increased effect of hydration (Karato, 2012), the presence of partial melt (Anderson & Sammis, 1970; Kawakatsu et al., 2009), and/or the enhanced effects at near sub-solidus conditions on seismic waves (Yamauchi & Takei, 2016). The debate centers around which of these explanations might be in operation and how widely they apply.

Partial melt is an attractive possibility given that it provides an explanation for a wide range of observations with different sensitivities (Rychert et al., 2020). Partial melt is likely to exist in the asthenosphere, in particular near mid-ocean ridges and volcanic arcs where the volcanic systems must be fed by mantle melting (Anderson & Sammis, 1970). However, further away from volcanic plate boundaries its presence is debated (Kawakatsu et al., 2009; Priestley & McKenzie, 2006; Rychert et al., 2005). The amount of melt and its location is vital to our understanding of how the lithosphere-asthenosphere works, as the presence of partial melt is predicted to reduce the viscosity of the asthenosphere (Hirth & Kohlstedt, 1995; Jackson et al., 2006) and could also facilitate plate tectonics (Rychert et al., 2005, 2007). However, different geophysical techniques with different sensitivities and resolutions have imaged anomalies that have been interpreted as melt in many forms (Rychert et al., 2020). For instance beneath Mid-Ocean Ridges, seismic surface wave studies have interpreted a broad, hundreds of kilometers wide, melt triangle beneath the ultrafast spreading East Pacific Rise at 17°S (Dunn & Forsyth, 2003; Forsyth et al., 1998) and the intermediate spreading Juan De Fuca Ridge (Bell et al., 2016; Gao, 2016), while other studies have imaged smaller scale and discrete melt zones beneath the slow spreading equatorial Mid-Atlantic Ridges on the order of 100–200 km wide (Harmon et al., 2020). The magnetotelluric (MT) method has typically imaged smaller and more discrete low resistivity zones interpreted as focused melt regions beneath the fast spreading East Pacific Rise at 9°N and the ultraslow spreading Mohns Ridge (Johansen et al., 2019; Key et al., 2013) that are typically <100 km wide, although a broader region >200 km was inferred beneath the East Pacific Rise at 17°S (Evans et al., 1999). Further off-axis, layered and/or pervasive melt in the asthenosphere has been inferred based on the imaging of discontinuities by scattered waves that require sharp drops in seismic velocity with depth (Kawakatsu et al., 2009; Rychert & Shearer, 2009, 2011; Tharimena et al., 2017). Active source seismic studies also find strong reflectors near the expected base of the tectonic plate that have been interpreted as channelized melt (Mehouachi & Singh, 2018; Stern et al., 2015). Similar channelized structures have also been interpreted from thin low resistivity zones at 60–80 km depth (Naif et al., 2013; Wang et al., 2020). Whether or not differences among the inferred shape and location of melt are an artifact of resolution and sensitivities of the individual methodologies or representative of real Earth structure has remained unclear.

The complementary resolution and sensitivities of MT and seismic imaging techniques offer a promising means of probing Earth's physical properties to examine the thermal structure and the presence of partial melt. The Earth's mantle is primarily composed of olivine and pyroxene, and the conductivity of these minerals has a strong temperature dependence (Gardés et al., 2014; Naif et al., 2021), enhanced by the presence of conducting fluids such as partial melt (Naif et al., 2021; Ni et al., 2011) and the presence of water and other crystallographic defects in the olivine mineral lattice (Gardés et al., 2014; Naif et al., 2021). Water and other volatiles such as CO_2 are also thought to significantly increase the conductivity of the fluid and therefore the overall conductivity of the mantle if present (Ni et al., 2011; Sifre et al., 2014). On the other hand, seismic velocities are dependent on temperature and pressure (e.g., Stixrude & Lithgow-Bertelloni, 2005), followed by the presence of partial melt (Clark & Lesher, 2017; Hammond & Humphreys, 2000), particularly for shear velocity, and are relatively insensitive to the presence of water as a crystallographic defect (Abers et al., 2014) or as a component of the partial melt. These differences mean that the two methods together have the potential to better constrain the thermal properties of the mantle, the presence and amount of partial melt, and the amount of hydration in the melt.

There have been two main approaches to cooperative or simultaneous joint inversion of electromagnetic and seismic data: (a) Inversion based on underlying petrophysical or empirical relationships between velocity and conductivity (Abubakar et al., 2012; Jegen et al., 2009; Sun & Li, 2016; Takougang et al., 2015) and (b)

inversion based on model gradient approaches, for example, forcing model changes in velocity and resistivity either in the same sense, the opposite sense, or with no change in one of the models (Bennington et al., 2015; Gallardo & Meju, 2004; Haber & Oldenburg, 1997; Moorkamp et al., 2011; Zhang et al., 2020). The petrophysical or empirical approach requires either accurate models of the physical properties of the rocks (Gardés et al., 2014), an (ideally) relatively simple system that can be captured with simple linear or polynomial fits to data (Jegen et al., 2009), or a guided fuzzy *c*-means clustering operator (Sun & Li, 2016), which is more likely the case in locations with limited compositional and thermal variation. However, the success of this approach depends strongly on the accuracy of the prior information and laboratory measurements, which is specific to the area of interest since the relationship between velocity and conductivity is not universal. The model gradient approach, such as cross gradient (Gallardo & Meju, 2004) and normalized cross gradient (Zhang et al., 2020), on the other hand, presumes that the gradient of resistivity structures is positively or negatively correlated with the gradient of velocity structures. The minimization of model gradient or cross-gradient can also be satisfied automatically where zero gradient is required by one or both data sets. In contrast with the petrophysical approach, the gradient method is more generic. The cross-gradient approach is probably more useful for detecting regions where the physical and chemical properties of the Earth result in seismic and resistivity anomalies that would not necessarily align. For instance, the presence of small amounts of certain minerals such as magnetite in serpentine (Stesky & Brace, 1973) or graphite (Frost et al., 1989) and other highly conductive minerals would generate a strong resistivity anomaly, but may not be volumetrically significant enough to have a strong seismic signature. Choosing between these two approaches or other approaches using Monte Carlo inversions (Moorkamp et al., 2010) is dependent on the details of the particular data sets and the structure involved. Combining the two approaches is possible, and exhibits enhanced performance for structural similarity in the joint inversion (Colombo & Rovetta, 2018; Guo et al., 2020).

The Imaging the Lithosphere-Asthenosphere Boundary (I-LAB) experiments including: (a) Passive Imaging of the Lithosphere Asthenosphere Boundary (PI-LAB) experiment, (b) Experiment to Unearth the Rheological Lithosphere-Asthenosphere Boundary (EURO-LAB), and (c) the Central Atlantic Lithosphere-Asthenosphere Boundary (CA-LAB) experiment presented a unique opportunity for interpretation of MT and seismic data in order to understand the oceanic lithosphere-asthenosphere system at the equatorial Mid-Atlantic Ridge. We deployed 39 ocean bottom seismometers (OBS) and 39 ocean bottom magnetotelluric (OBMT) instruments on 0–80 Myr seafloor across the long offset Chain and Romanche as (Agius et al., 2018, 2021; Harmon et al., 2018, 2020; Hicks et al., 2020; Rychert et al., 2021; Saikia et al., 2020, 2021; Wang et al., 2019, 2020), allowing us to sample a wide seafloor age range in one experiment. The OBS and OBMT were co-located (within 1–2 km), in three lines perpendicular to the ridge (Figure 1). The experiment was designed to image the uppermost mantle beneath the ridge system and examine the evolution of the oceanic lithosphere-asthenosphere system and the nature of the lithosphere-asthenosphere boundary.

Here, we focus on two results for developing a structurally consistent model of the oceanic lithosphere-asthenosphere system, the three-dimensional (3-D) shear-wave velocity model from Rayleigh wave tomography and the two-dimensional (2-D) MT inversions from the two southernmost lines (Figures 1 and 2). The shear velocity model images a high-velocity lithosphere, and several punctuated low-velocity zones (<4.2 km/s) in the asthenosphere, that were interpreted as melt (Harmon et al., 2020). Near the ridge axis, asthenospheric low-velocity zones are attributed to sub-ridge upwelling (anomalies A and E in line I and line II, respectively, in Figure 2), while further off-axis the low-velocity anomalies are attributed to melting due to upwelling caused by small scale convection (anomalies B, C, and F in Figure 2; Harmon et al., 2020; Wang et al., 2020). The MT result images similar structures to the surface wave model, for example, a high resistivity lithospheric lid ($\log_{10}(\rho) > 2$) and several low resistivity anomalies ($\log_{10}(\rho) < 1$) in the asthenosphere (anomalies A, B, C, D, E, and F in Figure 2; Wang et al., 2020). In line I, there is good agreement with the depth (50–80 km) and lateral extent (~100–200 km) of the low resistivity anomaly and low seismic velocities (anomalies B and C) as well as evidence for a high resistivity, high-velocity lithospheric drip (anomaly D) that extended from 50 to 150 km depth. However, in line II (Figures 2b and 2d), the agreement in terms of the shapes of the anomalies is less remarkable, specifically anomaly F, where the conductive anomalies suggest a channel structure <20 km thick extending from the ridge to 30 Myr seafloor, while the surface wave anomaly resembles a simple oval ~200 km wide from 50 to 80 km depth. In addition, anomaly E is deeper in the resistivity model, >100 km depth, than in the shear velocity model, where it extends from 50 to 100 km depth. While in line I, anomaly A is shallower at ~30 km depth and smaller, <50 km wide,

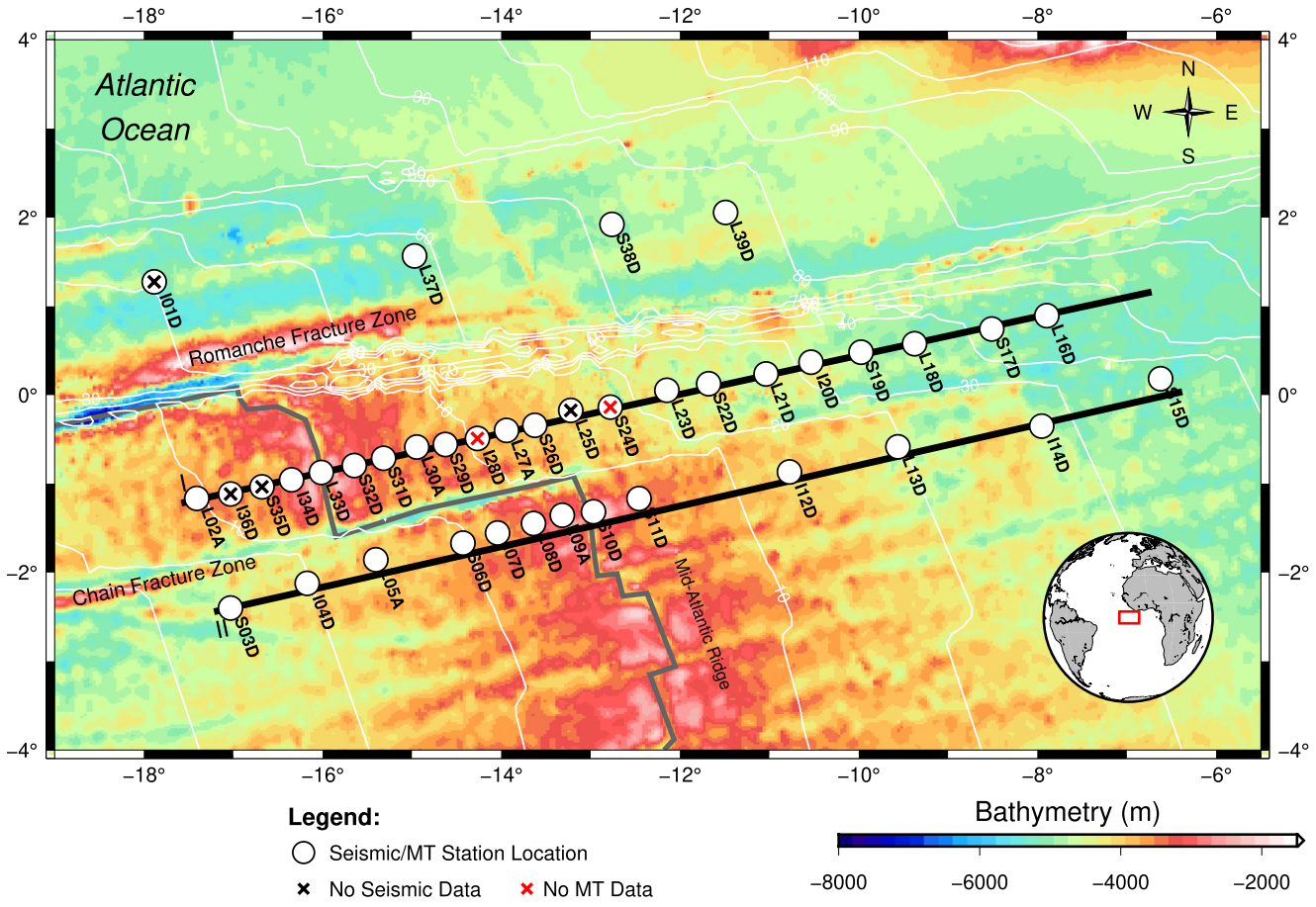

Figure 1. Map of the Passive Imaging of the Lithosphere Asthenosphere Boundary (PI-LAB) study region (Harmon et al., 2020). Circles indicate stations for seismic and magnetotelluric (MT) locations with names indicated. MT stations are within 1–2 km of the seismic stations. Bold black lines I and II indicate transects used in this study. Background colors indicate bathymetry (Smith & Sandwell, 1997), white contours indicate seafloor age from Seton et al. (2020), and thick, dark gray line indicates the location of the Mid-Atlantic Ridge. Red box in inset map indicates study area.

in the resistivity model than in the shear velocity model, where it is located at 50–80 km depth and 150 km wide. In other words, while there is some similarity in the lateral locations of the anomalies, the exact depth and morphologies are somewhat different.

Subsequent studies support the existence of these anomalies and suggest that apparent discrepancies may be artifacts of resolution. For example, S-to-P receiver functions support the existence of the anomalies (Rychert et al., 2021). The receiver functions image discontinuities associated with sharp velocity decreases with depth above the locations of the low shear velocity anomalies E, C, and F in the asthenosphere and also the locations where the low resistivity anomalies gradually decrease with depth in the asthenosphere (near anomaly E and directly beneath F; Rychert et al., 2021). In addition, a short period Rayleigh wave tomography study, which had better resolution in the upper 60 km than Harmon et al. (2020), imaged a shallower anomaly for anomaly A beneath line I, more consistent with the resistivity model (Saikia et al., 2021). The differences between the surface wave models suggest that there are several possibilities for shear-wave velocity models that will fit the Rayleigh wave data. Some of these shear velocity models could also be consistent with the anomaly structure of the resistivity models as well, noting that the MT method is preferentially sensitive to conductors, such as the anomalies C and F at the LAB depths. Therefore, the primary motivation of this study is to find a satisfactory shear velocity model that is also consistent with structural information from the resistivity models.

Here, we jointly consider the Rayleigh wave phase velocities and the MT data to evaluate differences and similarities between the seismic and MT anomaly structures, in particular to determine an Earth struc-

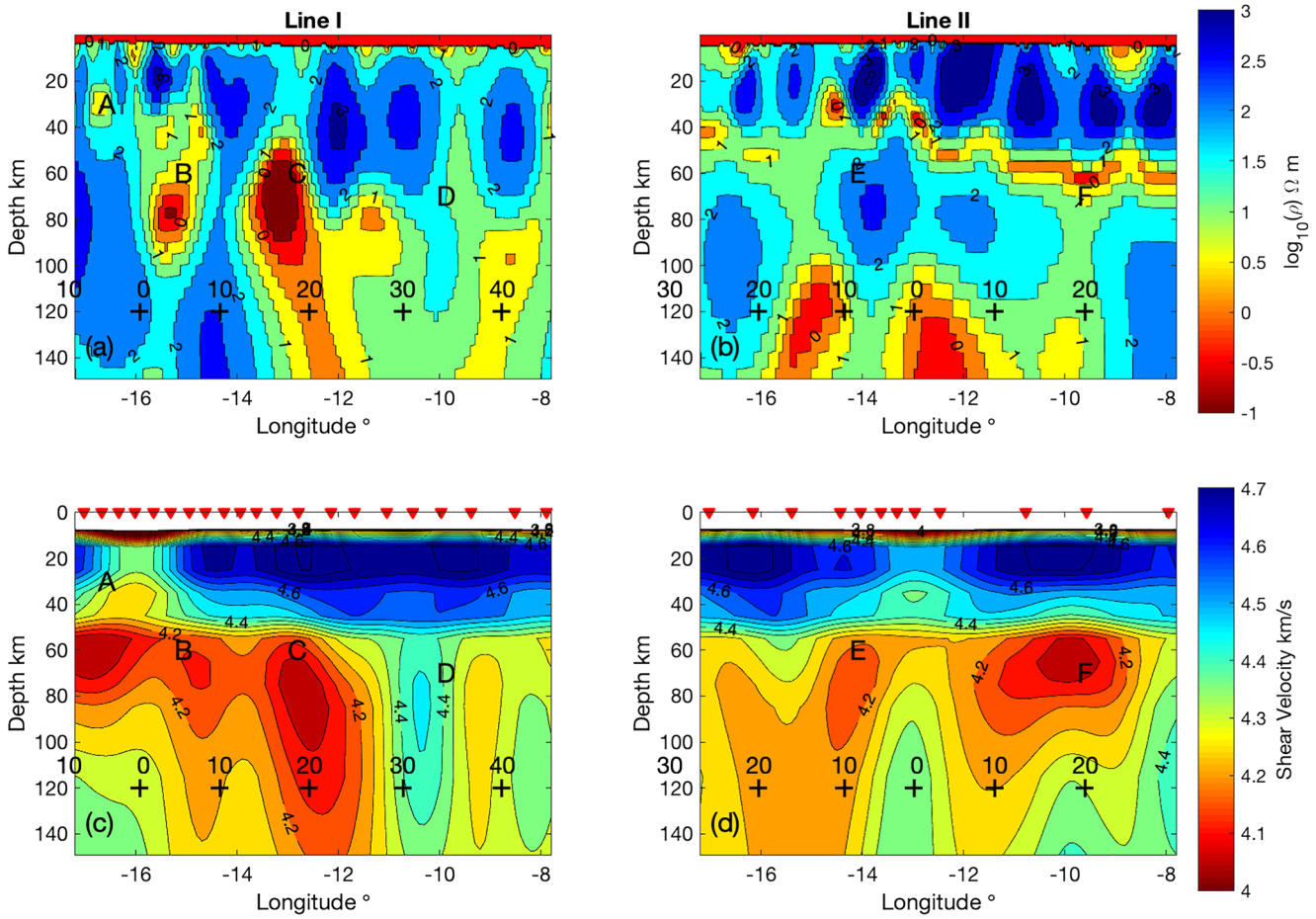

Figure 2. Resistivity model and shear-wave velocity model from previous work. Panels (a) and (b) show contoured resistivity transects from line I and line II, respectively, from Wang et al. (2020). Contour interval is 0.5 log units. Panels (c) and (d) show contoured shear velocity transects for lines I and II, respectively, from Harmon et al. (2020). Contour interval is 0.05 km/s. Anomalies A, B, C, D, E, and F from Harmon et al. (2020) are indicated. Red triangles show seismic/magnetotelluric (MT) station locations along the lines. Crosses at 120 km depth in plots indicate the seafloor age, in Myr, with 0 indicating the ridge location.

ture that can satisfy both data sets within data errors. We compare the models one-to-one to develop an empirical relationship between the two. Since the observed relationship is very similar to laboratory-based predictions for shear velocity and resistivity, we proceed using the laboratory-based relationship to translate the MT resistivity to shear-wave velocity. We use the MT-derived shear velocity model as the new starting model for the surface wave tomography inversion. This approach assumes that the structure within the resistivity model is closer to the true Earth structure, which may be the case, for example, if a thin channel structure exists, which surface waves would not be able to resolve without prior knowledge (e.g., Rychert et al., 2020). We discuss the validity of this assumption in the discussion section. Finally, we compare the models to petrophysical predictions for Earth properties in order to constrain temperature, the amount of partial melt, and the amount of hydration, carbonization or sulfide weight percentage of the partial melt in the asthenosphere.

2. Methods

MT data were inverted by Wang et al. (2020), which we briefly summarize here. The determinant of the MT impedance tensor was used to invert logarithmic apparent resistivity and linear phase along 2-D transects (line I and line II). The approach was chosen to minimize 3-D coast effects from the nearby African coast (Wang et al., 2019). For the period range chosen, 26–26,225 s, data quality and 3-D distortion were examined, and data points with visible 3-D distortion were excluded in the inversions. The impedance polar diagrams of the final selected data points were nearly parallel on either side of the Chain fracture zone in

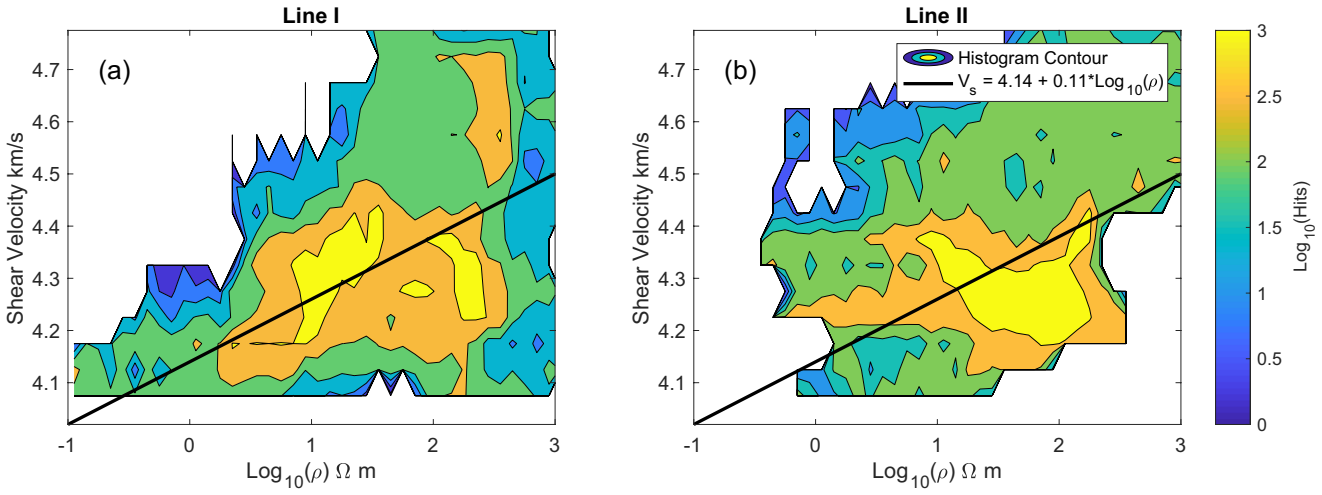

Figure 3. Cross-plot histograms of resistivity and shear-wave velocity from previous work (Harmon et al., 2020; Wang et al., 2020). Panels (a) and (b) shows the histograms for line I and line II, respectively. Black line indicates preferred linear relationship from petrophysical modeling shown in Figure 4.

lines I and II (Wang et al., 2020). Nevertheless, there may still be some 3-D effects due to fracture zones and/or ridges that influence the model, which we address in the discussion section. Forward calculations and inversion were performed using the MAR2DEM code (Key, 2016), modified to accept determinant data as an input (Wang et al., 2021). Inversion of MT data with this approach is less dependent on the starting model than surface wave inversion due to the diffusive nature of electromagnetic fields and the smoothness and regularization of the inverse problem. Here, we focus on varying the starting model for the shear velocity inversion based on structural information from the resistivity data, but not vice versa. We refer to this as resistivity structure guided shear velocity inversion.

We first establish a relationship between shear velocity and resistivity in our study area. We use two transects through the 3-D shear-wave velocity model of Harmon et al. (2020) in the same locations of the two 2-D resistivity model transects of Wang et al. (2020). We make cross-plots separately for the two lines. Cross-plots of the data suggest a linear relationship between the two data sets, but with scatter (Figure 3). The correlation coefficients of these cross-plots for line I is 0.43 ± 0.01 and line II 0.39 ± 0.01. A linear regression of line I between shear-wave velocity (km/s) and resistivity ($\log_{10}(\rho)$), yields a solution of $V_s = 4.19 \pm 0.02 + 0.10 \pm 0.02 \times \log_{10}(\rho)$, while for line II, $V_s = 4.22 \pm 0.02 + 0.08 \pm 0.02 \times \log_{10}(\rho)$ and for line I and II combined $V_s = 4.21 \pm 0.02 + 0.09 \pm 0.02 \times \log_{10}(\rho)$.

We also consider predictions from laboratory petrophysical relationships between shear velocity and resistivity for a half-space cooling model based on the error function solution to the conductive heat transfer equation (Parker & Oldenburg, 1973; Turcotte & Schubert, 2002). To calculate the temperature structure, we assume a thermal diffusivity of 1×10^{-6} m^2 s^{-1}, and a mantle potential temperature of 1350°C calculated for seafloor age from 0 to 40 Myr, the approximate range in of ages along lines I and II (Figure 4). To model the predicted shear velocity for a given temperature, pressure, and melt fraction we use the Very Broadband Rheology calculator (Havlin et al., 2021), assuming a peridotite mantle composition. We use the attenuation parameterization of (Jackson & Faul, 2010) that is included in the calculator and use an average across the surface wave period range used here, 18–143 s period. In this model, the addition of melt primarily affects shear velocity with ~2%–4% velocity reduction for 1% melt volume fraction depending on the dihedral angle (Takei, 1998). The model of Takei (1998) assumes that melt is interconnected, without necessarily prescribing a melt geometry. The associated predicted velocity reduction depends on wetness, which is a measure of the amount of grain-to-grain contact relative to the melt (Takei, 1998). Other models for the effect of melt on velocity exist based on different assumptions of melt geometry (Clark & Lesher, 2017; Hammond & Humphreys, 2000; Schmeling, 1985) which we evaluate in the discussion section. For resistivity, we use the relationship for hydrated mantle peridotite (Gardés et al., 2014) and a model for the conductivity of hydrous mantle melts (Ni et al., 2011). We then use the Hashin-Shtrikman upper bound to calculate the total resistivity of a melt bearing peridotite mantle (Ni et al., 2011), which, again, assumes interconnected

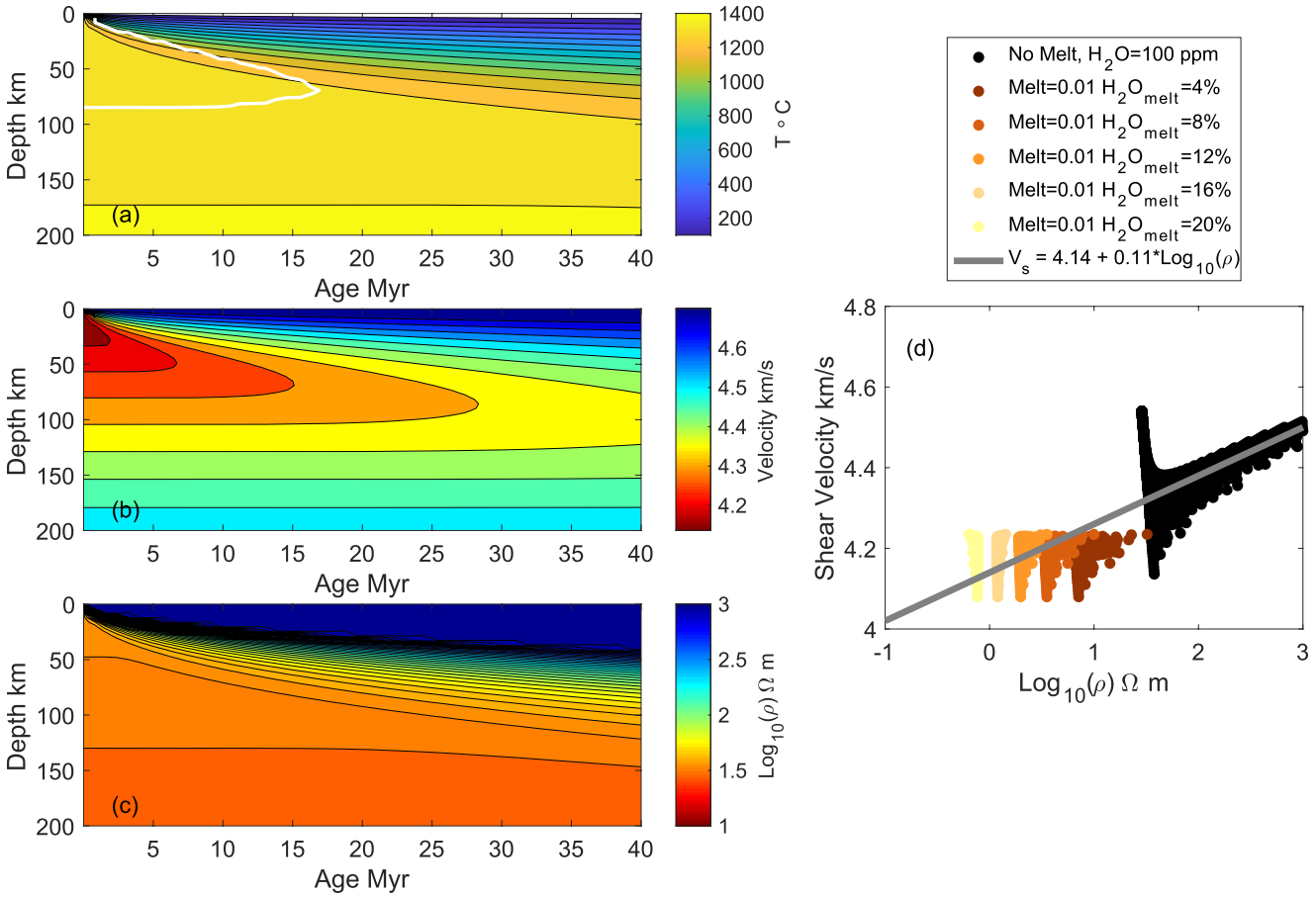

Figure 4. Petrophysical predictions for resistivity and shear-wave velocity for the half-space cooling model. Panel (a) shows the thermal structure for the half-space cooling model, (b) shows the predicted shear-wave velocity structure, and (c) shows the predicted resistivity structure from petrophysics calculated as described in the text. White line in panel (a) indicates the predicted melt triangle for 100 ppm water in a background mantle (Katz et al., 2003). Panel (d) shows the cross-plot of predicted resistivity and shear velocity without melt from panels (b) and (c) (black circles) and with a presumed melt fraction (0.01) containing different amounts of water (4%–20%), within the predicted melt triangle (yellow and brown circles). Gray line in panel (d) shows preferred linear relationship between resistivity and shear velocity based petrophysical modeling presented here and consistent with the cross-plot histograms presented in Figure 3.

melt. The predictions for an example case with 100 ppm water content in the background mantle and 1% melt in the melt triangle and variable amounts of water in the melt from 4 to 20 weight % are shown in Figure 4. We perform a linear regression on the melt-free mantle data points (black dots, Figure 4), and find a relationship of $V_s = 4.14 \pm 0.02 + 0.11 \pm 0.01 \times \log_{10}(\rho)$. This relationship is very similar to the one derived for the cross-plot in line I; the velocity intercept is 0.05–0.06 km/s lower than in our cross-plot, and the slope is only 0.01 km/s/$\log_{10}(\rho)$ higher than in the cross-plot. Given the similarity between the two and that the petrophysical line visually fits the data from the shear velocity and resistivity inversions, we opt to use the relationship from the petrophysical modeling.

We use the aforementioned petrophysical relationship to translate the resistivity model (Figures 2a and 2b) to shear-wave velocity, creating a new starting model (Figures 5c and 5d) for the shear velocity inversion. We then invert the phase velocities from 18 to 143 s period from Harmon et al. (2020) sampled along lines I and II, for shear velocity as a function of depth, sampling at every point, 0.1°. We calculate the partial derivatives relating Rayleigh wave phase velocity to shear velocity using the Computer Programs in Seismology package (Herrmann, 2013), and we assume a fixed V_p/V_s ratio of 1.8, which is consistent with the Preliminary Earth Reference Model (PREM), a global one-dimensional (1-D) seismic velocity model (Dziewonski & Anderson, 1981). We include a seawater layer along lines I and II in the model based on the local bathymetry. We use a damped least squares inversion and assume an a priori model error of 0.2 km/s following choices from previous work (Forsyth & Li, 2005; Harmon et al., 2020). We replace the upper 5 km of the model

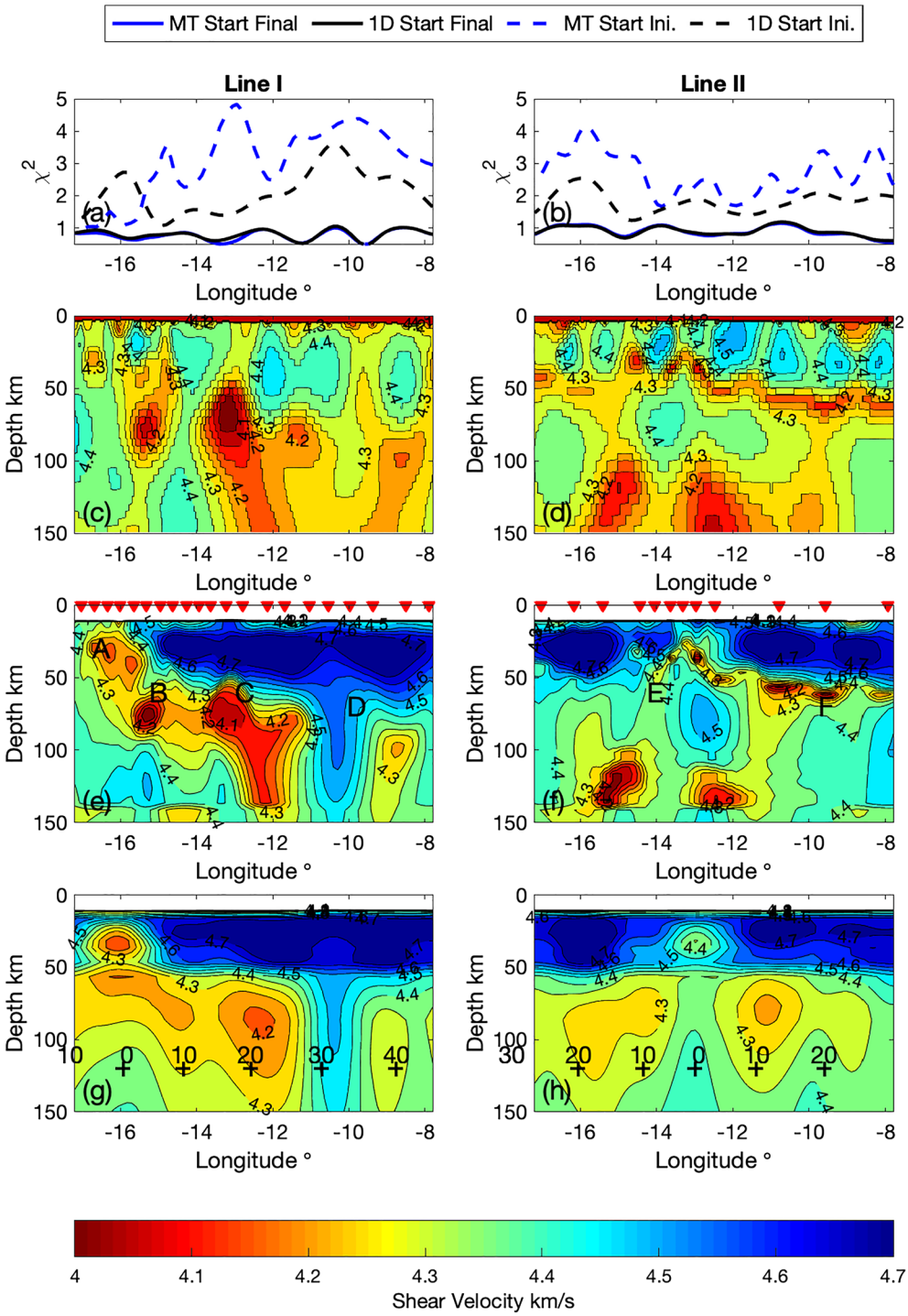

Figure 5. Shear-wave velocity inversions based on resistivity predictions. Panels (a) and (b) show misfit along lines I and II using normalized chi-square. The solid black and blue lines are almost coincident, indicating nearly identical fits. Panels (c) and (d) show the shear-wave velocity models that result from translating the resistivity model shown in Figure 2 to velocity using the linear relationships based on petrophysical modeling. Panels (e) and (f) show the shear-wave velocity inversion results using panels (c) and (d), respectively, as starting models. Red triangles show seismic/magnetotelluric (MT) station locations along the lines. Panels (g) and (h) show the shear velocity inversion results using the 1-D starting model from Harmon et al. (2020) and the smoothing, damping, and model parameterization used here. The model shown in panels (g) and (h) is for comparison purposes. It is different than that shown in Figure 2 panels (c) and (d) from Harmon et al. (2020) because we used a finer depth parameterization here in order to capture the fine scale structure of the resistivity model. Contour interval is 0.05 km/s. Asthenospheric anomalies A, B, C, D, E, and F from Harmon et al. (2020) and Wang et al. (2020) are labeled for reference. Crosses at 120 km depth in plots indicate the seafloor age, in Myr, with 0 indicating the ridge location.

beneath the water layer with average crustal values (3.5 km/s) from the 1-D model of Harmon et al. (2020). The model is parameterized every 5 km in depth down to 400 km. This parameterization is finer than that presented in Harmon et al. (2020) (Figure 2). The finer parameterization is necessary to capture the smaller scale variations in the resistivity model. Therefore, we also present an inversion using the 1-D starting model used in Harmon et al. (2020), but with the 5-km thick layers down to 400 km depth used here for comparison purposes (Figure 5).

We next determine the physical properties that explain the resulting anomalies including temperature, melt fraction and volatile content of the melt. These quantities can trade off with each other and multiple combinations can fit the data, and therefore, we use a grid search approach. We presume that the thermal structure at any given point along each line is similar to the predicted thermal structure from the half-space cooling model calculated above, but allow the effective seafloor age and corresponding thermal structure, resistivity and shear velocity to vary. The effective age of the seafloor (e.g., lithospheric thickness) could be older due to "drips" (as in anomaly D) or younger if the lithosphere is thinned due to upwelling. In other words, although seafloor age is known at each profile, we search over the effective age of the seafloor given that our previously published models suggest that the age progression of the lithosphere might not be monotonic everywhere. We calculate the half space cooling thermal structure for seafloor from 0 to 40 Myr age in 1 Myr intervals as described above. The thermal models have an adiabatic gradient added to them, and as above, we assume a mantle potential temperature of 1350°C. We do not vary the mantle potential temperature to minimize the free parameters in the grid search. We calculate the predicted shear velocity and resistivity for each 1 Myr age interval of the thermal model. For all locations where temperatures are predicted to be >1100°C we also calculate shear velocity and resistivity for a grid of melt fractions, melt water contents at the corresponding depth/pressure values using the relationships described above. For our grid we perform calculations for melt from 0.00 to 0.07 at 0.001 increments below 0.01 and at 0.005 increments above 0.01 and melt water contents from 0 to 30 weight % in 1% increments. This creates the grid for comparison to our models. We then examine the regions of our model that cannot be explained by temperature alone, specifically, where the shear velocity is <4.4 km/s and $\log_{10}$ resistivity is <1.5 (<30 Ωm), which are the nominal limits of the melt free predictions of the half-space cooling model (black dots, Figure 4). We perform a grid search over melt fraction, melt water content, and apparent seafloor age/temperature for each point in lines I and II. We then determine the chi-square residual between the observed resistivity and shear velocity with the predicted resistivity and shear velocity at the same depth in each thermal structure from 0 to 40 Myr. The chi-square residual is used to determine goodness of fit assuming an a priori standard deviation of 0.05 km/s for the shear velocity model and 0.10 $\log_{10}$ (Ωm) for the resistivity model. A value of melt, melt hydration and temperature is considered acceptable if the chi-square value is <1 for both the shear velocity and resistivity data. For most points, there are many combinations of melt, melt hydration, and temperature that satisfactorily fit the data. The optimum value is the minimum summed value of the chi-square values for resistivity and shear velocity. We present the error as the maximum parameter value minus the minimum acceptable parameter value divided by 2 for melt, melt water content, and temperature, which is the 95% confidence limit assuming symmetric error surfaces. We acknowledge that this choice of reporting does not give a sense of the trade-offs in these parameters.

3. Results

The shear-wave velocity structure derived from translating the MT models to seismic velocity according to the petrophysical predictions (Figures 5c and 5d) closely resembles the MT models (Figures 2a and 2b), which is to be expected. The shallow white regions in Figure 5 are due to the imposed water layer of 0.0 km/s in the model. The seismic velocities range from 4.5 km/s in the upper 20 to 50 km of the Earth, with a minimum of 4.03 km/s associated with the lowest resistivity regions. Strong lateral gradients are also visible in the starting model, with changes of 0.4 km/s over less than 50 km, particularly near anomaly C. The line II model has low-velocity channels across the transect at 20–70 km depth and several high-velocity regions in the asthenospheric mantle.

When we use the shear-velocity model derived from MT (Figures 5c and 5d) as the starting model for the surface wave inversion we find a new shear-wave velocity model (Figures 5e and 5f) that more closely resembles the MT models than the previously published model (Figure 2). The highest velocities are up to 4.81 km/s and found in the fast lid, while the minimum velocity is 4.00 km/s, found in anomaly B. The high-velocity lid is more continuous than in the starting model but follows a similar pattern of increasing

thickness away from the ridges in both lines I and II. In the asthenosphere, low-velocity structures from the starting model are also retained. Specifically, the channel structures in line II, near anomalies E and F, are retained throughout much of the model, particularly in the east near anomaly F, with similar velocities (~4.0 km/s) to those in the starting model. The deep low-velocity anomalies beneath anomaly E are also retained in the final model. Anomaly E from the model of Harmon et al. (2020), has been moved deeper into the mantle in the MT-derived starting model inversion, while anomaly F has been compressed into the channel structure. In line I, anomalies B and C are preserved, that is, velocity anomalies of ~4.0 km/s, as in the starting model. Anomaly A is more pervasive beneath the ridge than in the MT starting model. Anomaly D is also enhanced in the shear velocity model, with a high velocity of 4.56 km/s relative to the starting model of 4.31 km/s at 100 km depth. The chi-square values indicating goodness of fit to the data are shown in Figures 5a and 5b and are ~1 or less for most of the profile indicating a fit that is within error. This goodness of fit is similar to the values from Harmon et al. (2020).

When we use the 1-D starting model from Harmon et al. (2020) for the surface wave inversion, and the parameterization and damping used here we find similarities and differences in comparison to Harmon et al. (2020) that illustrate the range of possible models that fit the data (Figures 5g and 5h). A high-velocity lid is visible beneath the ridge and across the region that ranges from 20 to 60 km in thickness. It shows low velocities beneath the ridge, with a stronger and shallower low-velocity region beneath the ridge than in the model of Harmon et al. (2020), although in general the features are similar, and the magnitude of the named velocity anomalies are similar in general, <4.2 km/s but >4.0 km/s. These differences highlight the effect that even small changes in parameterization can have on the final model. The normalized chi-square fit to the data is shown in Figures 5a and 5b for lines I and II, respectively. The chi-square values are generally ~1 or less indicating that the model fits the data within error and has a similar fit to the model with the MT starting model. It is interesting to note, that prior to inversion (i.e., the 0th iteration), the fit of the 1-D model is generally better than the MT starting model (chi-square of ~2–3 vs. 4–5, blue dashed vs. black dashed Figures 5a and 5b). This is likely because the 1-D model originated from the best-fit 1-D average seismic model for the region. Both converge to very similar final chi-square values after the iterative inversion. The new shear-velocity model with the 1-D starting model presented in Figures 5g and 5h is primarily for comparison purposes. The goal of the study is to align the previously published shear-wave velocity and resistivity models, and so we do not discuss the model of Figures 5g and 5h further except for the purposes of resolution discussions.

The correlation between resistivity and shear-velocity after inversion is higher when the MT derived starting model is used in comparison to when the 1-D starting model is used. For the 1-D starting model inversion result with the finer parameterization used here, there is a slope visible in line I (Figure 6a), but there is less of a visible relationship in line II (Figure 6b). Visually, the cross-plots for the MT derived starting model inversion result are more linear, with more of a slope visible in both lines I and II (Figures 6c and 6d). The correlation coefficients between the resistivity model and the shear velocity model assuming a 1-D starting model presented here are 0.41 ± 0.01 and 0.29 ± 0.01 for lines I and II, in other words similar to that between the resistivity and the original shear velocity model presented in Harmon et al. (2020) above (0.43 ± 0.01 and 0.39 ± 0.01, respectively). The correlation coefficients are higher, 0.56 ± 0.01 and 0.62 ± 0.01 for lines I and II, respectively, for the shear-wave model resulting from the MT-derived starting model. With the two lines combined the correlation coefficient is 0.60 ± 0.01 (Figure 7).

We illustrate the behavior of the effect of varying the amounts of melt and water in the partial melt and compare it to the V_s and resistivity histogram for both lines I and II (Figure 7). We use the thermal structure from the half-space cooling model shown in Figure 4 but now allow partial melt at 0.1%, 1.0%, and 3.0% where the mantle temperature exceeds 1100°C. We also vary the amount water in the partial melt between 4% and 20%. The smallest amount of partial melt reduces the seismic velocity by <<1% in most cases, while the resistivity is reduced by ~0.6 $\log_{10}$ (**Ω**m) over the range of water contents presented here. At 1% melt the shear velocity is reduced by ~2%, and the effect of increased water content is stronger, reducing the resistivity up to ~1.5 $\log_{10}$ (**Ω**m) at the highest water contents. Finally, at 3% melt, the velocity is reduced by 4%–5% and the resistivity reduction is up to ~2.1 $\log_{10}$ (**Ω**m). The span of partial melt and melt water contents considered here also generally spans the range of most of the shear velocity and resistivity values from our inversions, i.e., the petrophysical values overlie the peak in the histogram. There is a slight bias in the seismic velocities with a longer tail toward higher values.

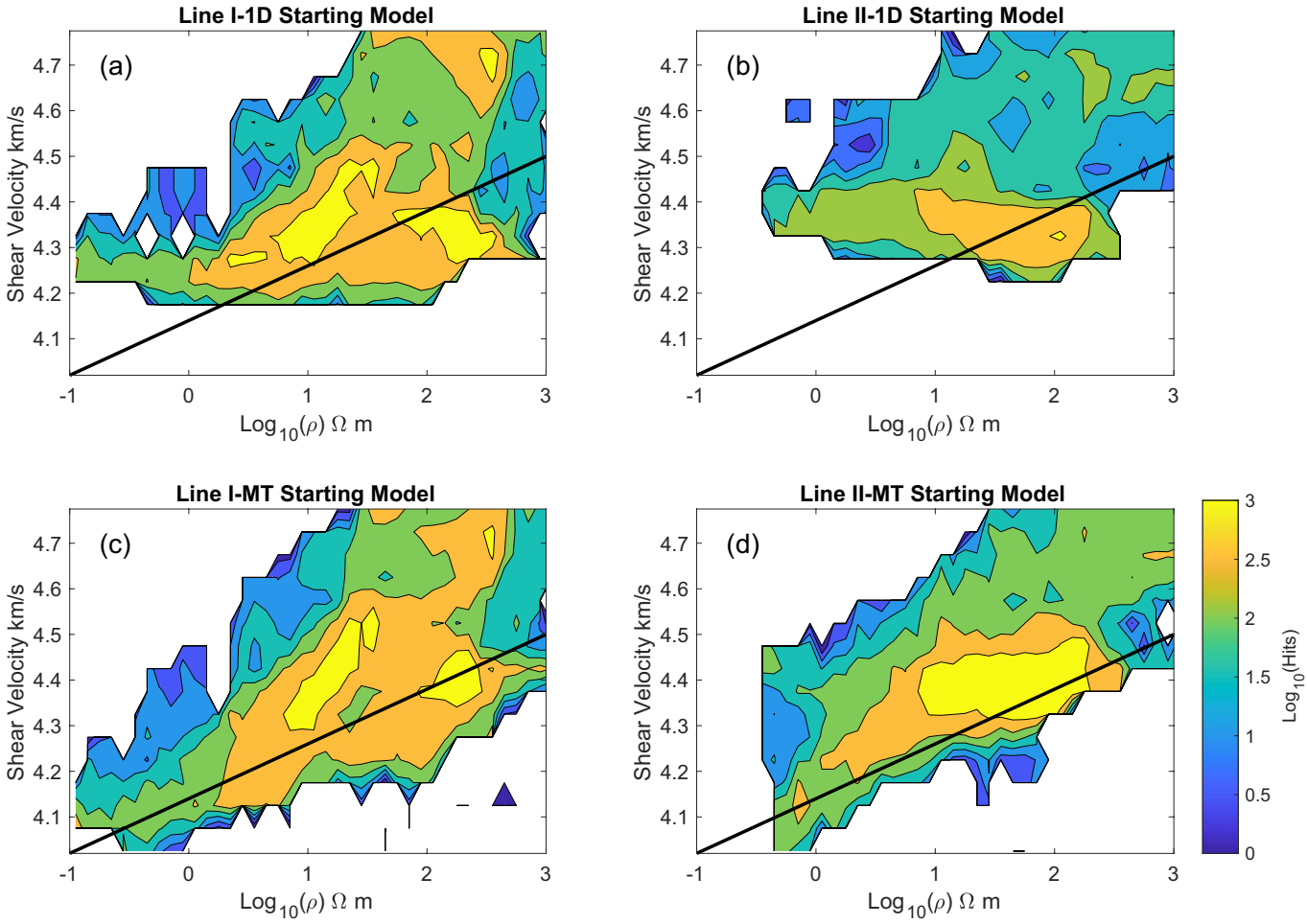

Figure 6. Cross-plot histograms of resistivity and shear-wave velocity models. Panels (a) and (b) show the cross-plot histograms for line I and line II, respectively, for the shear-wave velocity model derived from using the 1-D velocity starting model from Harmon et al. (2020) and the damping, smoothing, and parameterization used here (Figures 5g and 5h). Panels (c) and (d) show the cross-plot histograms of the MT-derived shear-wave velocity model (Figures 5e and 5f). Black line indicates preferred linear relationship from petrophysical modeling shown in Figure 4.

Given the good general agreement between the petrophysical modeling and the shear velocity and resistivity model values, we map the amount of partial melt, water content of the melt, and temperature relative to the half-space cooling model onto the transects of lines I and II (Figure 8). We only perform this mapping where shear velocity is <4.4 km/s and $\log_{10}(\rho) < 1.5 \log_{10}(\Omega\text{m})$, which is the nominal lower limit of the melt free half-space cooling model (Figures 4 and 7). In line I we find partial melt contents up to 4%–4.5% near anomalies B and C and similar maximum values in line II for anomalies E and F. Lower values of partial melt <2% are needed near anomaly A and for most of the other regions, typically requiring <1%. The water content of the melts is typically <10 weight % for most (~60%) of the total anomaly area (colored regions in Figure 8), with the notable exception of anomaly C which requires up to 24 weight % water content to account for the low resistivity found in this region and anomaly B which requires up to 15 weight %. There are other smaller patches of high-water content visible near the edges of some of the regions, and within the channel of anomaly E. The temperature structure generally has cooler temperatures 1100–1200°C at depths <100 km and temperatures >1300°C at a greater depth. The grid search provides formal error bounds corresponding to our presumed data errors (Figure 9). The errors for the melt percentages are typically <1%, while error for water content of the melt is on average 4 weight %, and the average error for temperature is 26°C.

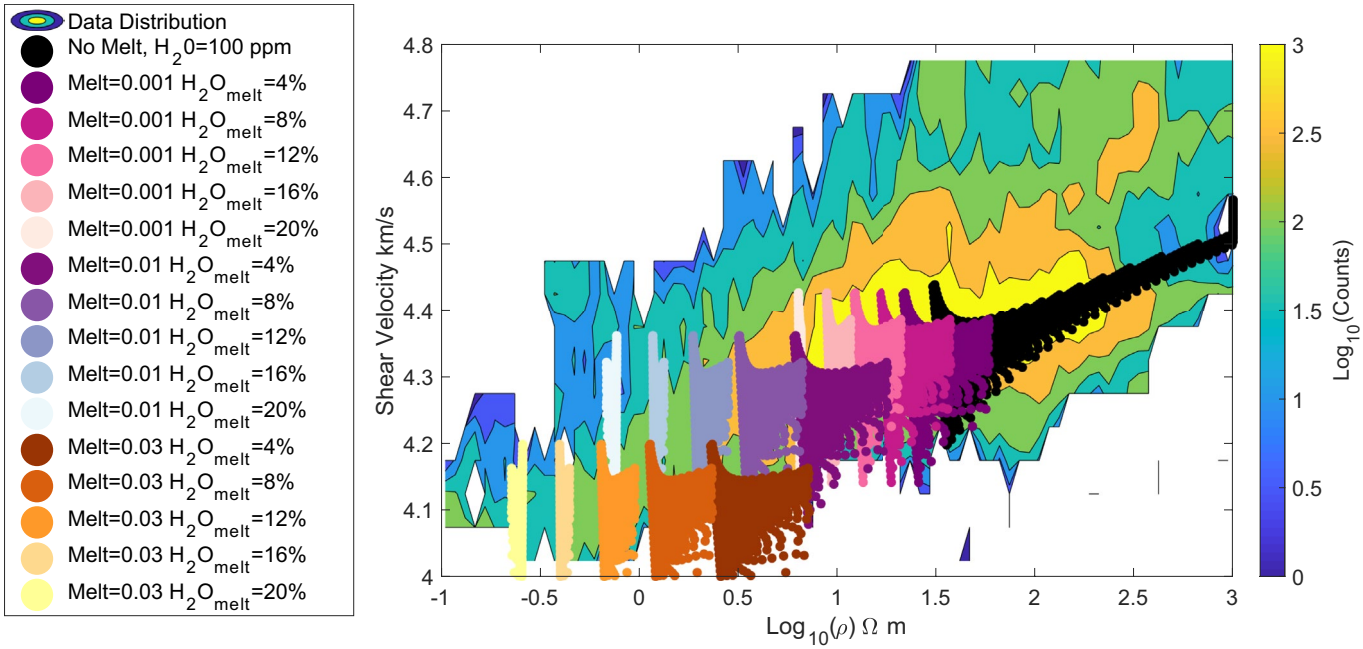

Figure 7. Cross-plot histogram of resistivity and shear-wave velocity from the MT-derived shear-wave velocity model for both lines I and II and petrophysical predictions. Purely thermal predictions are shown as black dots. Colored dots show predictions for various melt fractions and melt water contents. Legend indicates the amount of imposed disequilibrium melt fraction (0.001, 0.01, and 0.03) and water content of the melt in weight % (4%–20%).

4. Discussion

The inversion result from the MT derived starting model fits the phase velocity data within error. Initially, the misfit of the MT-derived starting model before inversion is only a factor of 2 greater than the misfit of the 1-D starting model before inversion in most places. This suggests general agreement between the MT-derived starting model and the phase velocity data. The inversion result using the MT-derived starting model fits the phase velocity data just as well as the shear velocity model of Harmon et al. (2020) which used a 1-D starting model and also the shear velocity model using the 1-D starting model and the finer parameterization presented here for comparison purposes. All of these have a normalized chi-square value 1 or less for most of the transects. The MT-derived shear-velocity model improved the visual agreement and correlation coefficient between the resistivity and shear velocity model.

Overall, many of the common features of the original studies are retained and several of the anomalies come into better agreement. For example, the MT-derived shear velocity model retains the thickening of the lithosphere and the drip feature at anomaly D observed in the Harmon et al. (2020) model. The lithospheric thickening with distance from the ridge is more pronounced in the MT-derived shear velocity model in comparison to that of Harmon et al. (2020), presumably a result of removing the 1-D influence on the model. Anomalies B and C are also retained in the MT-derived model, although anomaly B is more prominent than in the Harmon et al. (2020) study. In the asthenosphere, better agreement between the resistivity model and the MT-derived shear velocity model is achieved for the channel features in line II associated with anomaly F. Anomaly C in the MT-derived shear velocity model has a morphology more similar to the MT model than in the Harmon et al. (2020) model. Anomaly A shifts shallower than the Harmon et al. (2020) model and aligns better with a weak shallow anomaly directly beneath the ridge in the resistivity model. Anomaly E is deeper than that in the Harmon et al. (2020) model, again in better agreement with the resistivity model.

The differences in the shear velocity models here highlight some of the limitations of the approach. Specifically, inversion of Rayleigh wave phase velocities for shear velocity structure is non-unique, and this is well-known (Rychert et al., 2020) as many previous works have demonstrated that a variety of models can fit a given dispersion curve. The differences between the result of Harmon et al. (2020) (Figure 2), the result using the 1-D starting model with smoothing, damping, and parameterization of this study (Figures 5e and 5f) and the result

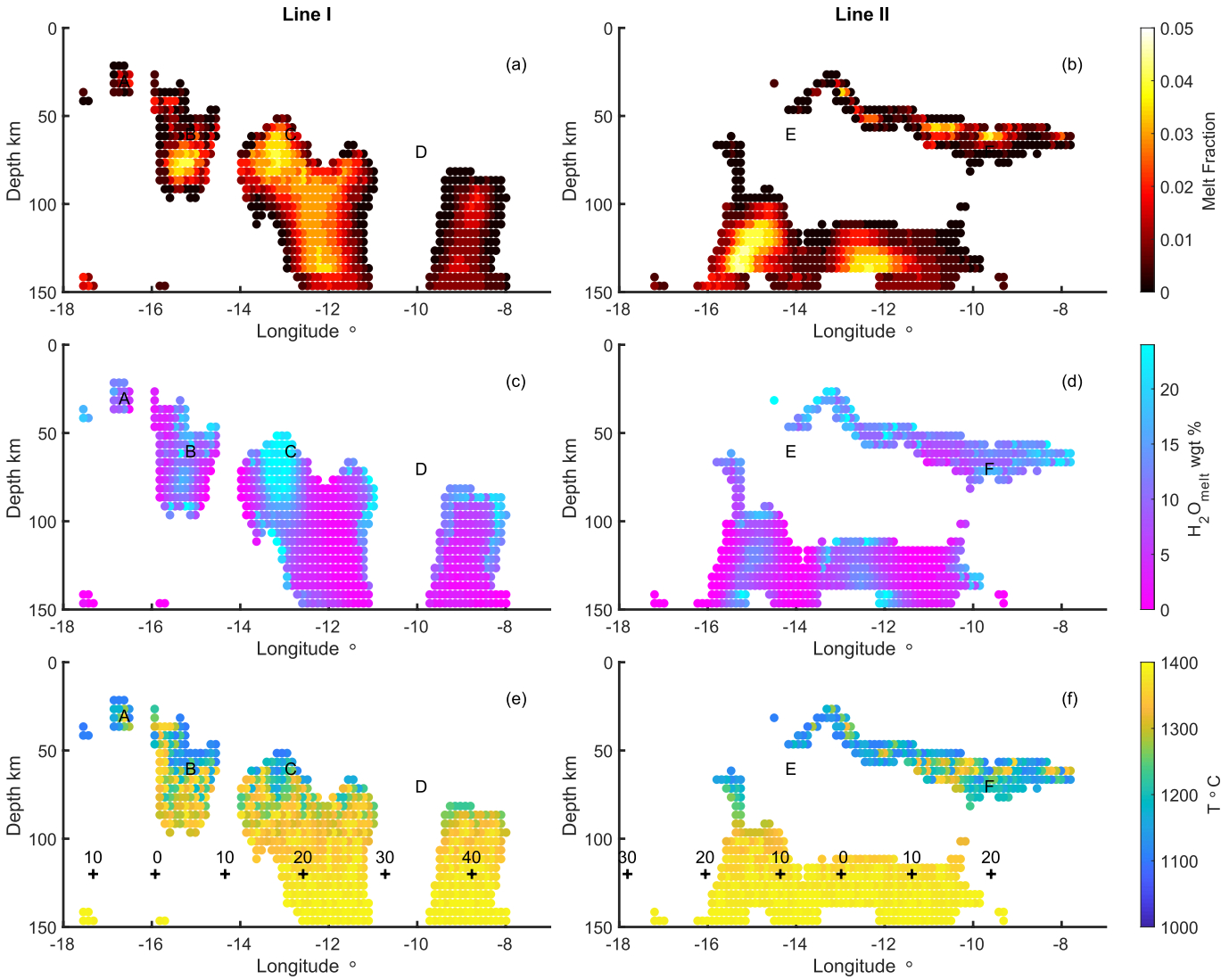

Figure 8. Results of grid search for partial melt, melt water content, and mantle temperature. Panels (a) and (b) show results for partial melt fraction, panels (c) and (d) show water content of the partial melt, and panels (e) and (f) show the result for temperature for lines I and II, respectively. Anomalies A, B, C, D, E, and F are labeled at the same locations as in Figure 2 for reference. Crosses at 120 km depth in plots indicate the seafloor age, in Myr, with 0 indicating the ridge location.

using the MT-derived starting model (Figures 5g and 5h) illustrate this fact again and highlight that the strength of an anomaly can vary from model to model depending on the starting model, even if similar damping is used and the same fit is achieved as was the case here. For instance, the MT-derived shear-wave velocity model includes velocities in anomalies B and C that are up to 1% slower in comparison with Harmon et al. (2020), which impacts interpretation in terms of the presence of partial melt. Suitable additional constraints are needed to determine which structure is the most likely, such as information from receiver functions or resistivity.

The cross-plots indicate that the shear-wave velocity and resistivity models are in good agreement with the petrophysics predictions for the half-space cooling model and variable partial melt concentrations and melt water contents. About 80% of the shear velocity data lie within 0.1 km/s of the petrophysical predictions for reasonable temperature structure, melt and melt water contents (Figure 7). The resistivity model is completely spanned by the petrophysical predictions. Shear velocity appears to be biased toward higher values, which may be a result of either the inversion process or a physical process. Shear-wave velocity inversions can trade off velocities at shallow depths with deeper asthenospheric anomalies, by compensating low asthenospheric values with higher lithospheric values. On the other hand, other physical effects such as depletion (Schutt & Lesh-

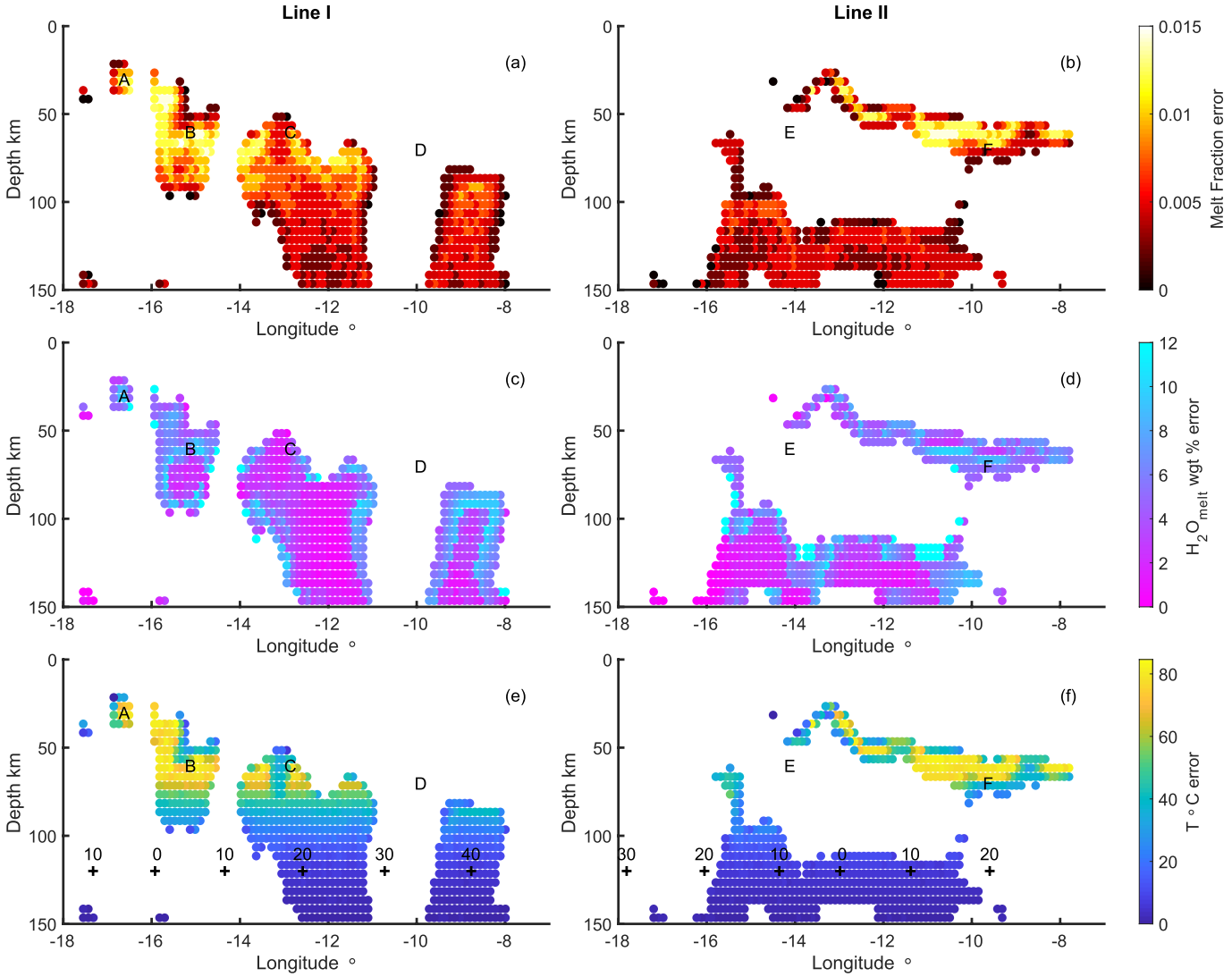

Figure 9. Error estimates of grid search for partial melt, water content of the melt and mantle temperature. Panels (a) and (b) show partial melt fraction error, panels (c) and (d) show water content of the partial melt error, and panels (e) and (f) show temperature error for line I and line II, respectively. Anomalies A, B, C, D, E, and F are labeled at the same locations as in Figure 2 for reference. Crosses at 120 km depth in plots indicate the seafloor age, in Myr, with 0 indicating the ridge location.

er, 2006) of peridotite through ridge melting toward more harzburgitic compositions (Hacker & Abers, 2004) could cause higher velocities by ~1%–2%. In addition, anisotropy could also enhance the apparent velocity by up to 1%–3% (Rychert & Harmon, 2017; Saikia et al., 2021). In reality, it is likely some combination of these physical effects and model artifacts which are not accounted for in the calculations used for predicting shear velocities.

In this work, we chose to force the shear velocity structure toward a closer match to the resistivity model, because the MT method has better resolution for certain features such as electrically conductive thin channels, which is an assumption that is worth examination. We presumed the resistivity model has better structural resolution, but this assumption has limitations, since the 2-D assumption for the resistivity model may break down. For instance, anomaly E is part of a larger 3-D velocity anomaly that extends to the south along the Mid-Atlantic Ridge in Harmon et al. (2020), and the depth of the anomaly is much greater in the resistivity anomaly, perhaps owing to issues of dimensionality. The deep conductive anomalies beneath anomaly E are also poorly resolved in the MT data (Wang et al., 2020), suggesting there is still some uncertainty about this particular location. Other observations, such as S-to-P receiver functions, suggest there may be a shallower shear velocity anomaly associated with anomaly E, which is necessary in order to produce a sharp velocity contrast in these regions (Rychert et al., 2021). In addition, the lateral extent

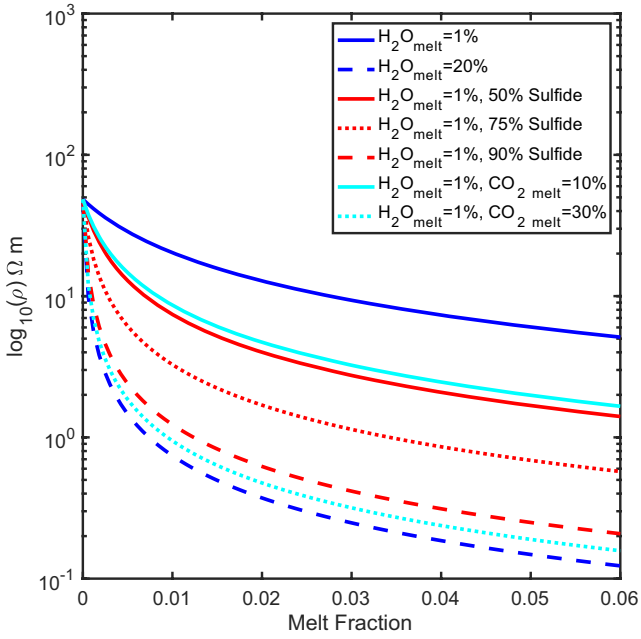

Figure 10. Effective resistivity predictions for water, CO_2 and sulfide in silicate melts as a function of melt fraction. We assume a solid mantle with 100 ppm water and disequilibrium melt at 1300°C. Legend indicates the respective water, CO_2 and sulfide concentrations. Melt with water only is shown as blue lines. Melt that includes water and CO_2 is shown as cyan lines and melt that includes sulfide is shown as red lines.

of the S-to-P discontinuity agrees well with the lateral extent of the Harmon et al. (2020) anomalies, suggesting this is a 3-D feature that is not well resolved in the 2-D MT inversion. However, given that we prefer the MT-derived shear-wave velocity structure for some of the major anomalies (A, B, C, D, and F), we proceed by interpreting our estimates for mantle melting and melt water content, bearing the limitations of the inversions in mind.

The thermal structure predicted from our grid search (Figures 8e and 8f) suggests relatively warm temperatures beneath anomalies B and C as well as the deeper parts of E (>1300°C), while anomalies A and F have relatively low temperatures (1100–1200°C). This variability is likely a result of the pressure dependence of the seismic waves. The low temperatures are generally consistent with the interpretation that the shallow anomalies, particularly the channel structures in F, are interacting with the base of the lithosphere (Harmon et al., 2020; Wang et al., 2020). The deeper, hotter anomalies (anomalies B and C) are also generally consistent with the interpretation of upwelling from depth associated with small scale convection.

The predicted melt fractions are in general agreement with our previous work from the region, considering the various assumptions. Our melt fraction of up to 0.04 agrees with the 0.01–0.07 values previously reported based on the resistivity model alone (Wang et al., 2020). It is higher than the 0.005 to 0.015 reported by the previous shear-wave velocity model (Harmon et al., 2020). However, this can be explained by two main differences: (a) The anomalies in the new shear velocity model presented here are up to 1% slower than those of the previous study (Harmon et al., 2020) and (b) we used the Takei (1998) relationship between melt and velocity here, which corresponds to about a 2% velocity reduction for 0.01 melt fraction in comparison to the 7.9% reduction for 0.01 melt fraction from the work of (Hammond & Humphreys, 2000) used by Harmon et al. (2020). Our melt fraction result of up to 0.04 is also consistent with the 6%–11% velocity drop with depth required by receiver functions after correcting for the maximum effect of temperature (Rychert et al., 2021), which would require melt fractions of 0.03–0.06 assuming the same melt-velocity relationship from Takei (1998) that we used here.

A different parameterization choice for the effects of melt on velocity due to different assumptions on the melt geometry could yield lower melt fraction requirements by the seismic constraints and still satisfy the resistivity model. The Takei (1998) model used here presumes interconnected melt, which permits current flow and affects resistivity, but does not prescribe a specific melt geometry rather using "wetness" and dihedral angle. Unconnected melt geometries such as isolated pockets (Schmeling, 1985) do not affect resistivity and so we can rule those out (Naif et al., 2021). Assuming interconnected films and organized cuspate tubules (Hammond & Humphreys, 2000), as used in Harmon et al. (2020), reduces the maximum amount of partial melt fraction to <0.02. Melt in the form of interconnected tubules and cuspate geometries (Hammond & Humphreys, 2000), which have a velocity reduction of 14.5% per 0.01 melt fraction would suggest even lower melt fractions (<0.01). Resistivity does not depend strongly on the geometry of connected melt. This is mostly due to the fact that the greatest resistivity reduction occurs at melt fractions <0.03, with a more gradual reduction in resistivity at higher melt fractions (Figure 10). However, since resistivity also has a strong dependence on the volatile content in the melt, the lower melt fractions predicted for the interconnected tubules and cuspate geometries could also satisfy the resistivity anomalies with additional volatiles. More work would be required to determine the most likely partial melt geometry and relationship for shear velocity reduction to place better constraints on the three-fold variation predicted from differing assumptions.

Predicted water contents are typically <10 weight % for the melt but are surprisingly high, up to weight 24%, in the centers of anomalies C and F. Simple fractional or batch melting calculations suggest that for a

typical MORB mantle source with 100 ppm and an average 6% melting of the mantle, water contents of the melt should be ~0.2 weight % (Workman & Hart, 2005). Higher water melt contents are possible for low degrees of partial melting, for example, <0.005 melt fraction yields >1% weight water for 100 ppm in the mantle source, and >7% weight water for 800 ppm in the mantle source. One possible explanation is that these off-axis anomalies represent coalesced low-degree melts of a moderately wet mantle with high water content. There is some geochemical evidence for a moderately wet mantle from basalts collected from the ridge segments in the study area, with estimated water contents that range from 110 to 770 ppm (~0.01–0.08 weight %) for the mantle source (Le Voyer et al., 2015). The advantage of this model in which volatile rich melts coalesce is that wet melts are stable and can persist in the mantle for long periods of time as has been suggested as an explanation for inferred melt channels beneath older oceanic lithosphere imaged by active source imaging (Mehouachi & Singh, 2018).

High CO_2 in the mantle melts instead of high-water content is another possible explanation for the low resistivities observed in region (Sifre et al., 2014). Carbonated peridotite is thought to exist in the mantle, although the abundance of carbon is relatively low, likely <100 ppm, as it is present in ancillary phases, rather than being hosted in olivine or pyroxene (Dasgupta & Hirschmann, 2010). Carbonated melts are generated and stable at greater depths, and only small degrees of partial melt are likely to be generated (<0.001 melt fraction; Dasgupta & Hirschmann, 2010; Hirschmann, 2010). However, the melts could percolate upwards and coalesce, generating higher CO_2 contents in the melt (Hirschmann, 2010). Figure 10 shows the trade off in effective resistivity for 1 weight % water in the melt, and 10% and 30% CO_2 by weight in the melt as a function of disequilibrium melt fraction assuming 100 ppm in the un-melted mantle background for a depth of 80 km and a temperature of 1350°C. The figure is for demonstrative purposes since; (i) melt fraction is imposed rather than generated using batch melting or fractional melting, (ii) we did not vary temperature as we did in the silicate case, and (iii) the melt may not necessarily be stable. At 30% CO_2 weight percent the resistivity is similar to the high-water content (20 weight %) case. However, geochemical estimates of CO_2 in the primary ridge basalts range from 104 ppm to 1.9 weight % (Le Voyer et al., 2019), which is much lower than the >30 CO_2 weight % needed to explain our results. To reach our high values, again aggregation of extremely low degree partial melts would be required, and this also cannot be the melt that directly erupts at the ridge.

Another possible explanation for the observed anomalies besides high water contents (>10%) is sulfide melts, which are extremely conductive, $>10^4$ S/m (Ducea & Park, 2000). Small amounts of sulfide melts can rapidly reduce the effective resistivity of the aggregate. To illustrate this we follow the parameterization of Ducea and Park (Ducea & Park, 2000), using the (Gardés et al., 2014) parameterizations for the solid olivine and the Ni et al. (2011) parameterization for the silicate melt. We assume a conductivity of 10^4 S/m for sulfide melts. Figure 10 shows a comparison between the effective resistivity for an olivine matrix with wet disequilibrium melts and also for sulfide/wet disequilibrium melt mixtures with predominately sulfide melt. Like the CO_2 case, this is for demonstrative purposes, without varying a full suite of parameters. A nearly pure sulfide melt has a similar resistivity as a silicate melt with 20% water, reaching values below 1 Ωm at <0.01 melt fraction. So, in this case, regions of high melt water contents in Figure 8, for example, anomaly C, could also be regions of high sulfide melt content. Given the bulk abundance of sulfur measured in basaltic glasses in the region typically <0.1 weight % (Le Voyer et al., 2015) and in <0.3 weight % in xenoliths from continents (Ducea & Park, 2000), it is unlikely that 0.04–0.05 sulfide melt fraction exists in the mantle. A more conservative sulfide melt fraction of ~0.01 could partially explain anomaly C (Hammond & Humphreys, 2000). There is also some evidence that melts from the nearby ridge segments are sulfur saturated (Le Voyer et al., 2015), and this may therefore suggest that sulfide melts may exist in higher abundance away from the ridge melt triangle where silicate melts are in high abundance. Sulfide melts have also been proposed to explain low seismic wave speeds in the asthenosphere (Helffrich et al., 2011). Further work is needed to test whether sulfide melts would be compatible with small-scale convection and explain our off-axis anomalies, as they have a higher density than silicate melts.

The melt anomalies inferred here extend to the base of our well-resolved region, ~150 km depth, which is greater than the 60–80 km predictions of a dry melting curve (Katz et al., 2003). This suggests that water or

CO_2 induced melting is occurring at depth or the presence of sulfide melts or some combinations are active to produce melts so deep. In addition, the largest melt fractions are associated with anomalies B, C, E, and F, which are far from the ridge axis. This suggests melt generation occurs away from the ridge either owing to off-axis small-scale upwellings, the presence of volatiles, or the combination of the two. Persistent melt near the base of the lithosphere and apparent channelization near anomaly F also suggests a role for water or other volatiles in the melts in order to stabilize them at relatively cool temperatures near the base of the lithosphere (Mehouachi & Singh, 2018).

Our joint seismic-MT constraints require melt fractions (>0.01) over large swaths of the asthenosphere mantle, several hundred kilometers, and hundreds of kilometers off the ridge axis. Such high percentages are not expected to persist over time and length scales that would enable seismic imaging (Spiegelman & Elliott, 1993). Yet, melt fractions >0.01 could be explained by a lack of a drainage route for the melt. Melt may coalesce at a permeability boundary at the lithosphere-asthenosphere boundary, as suggested by recent numerical models that include two-phase flow (Sim et al., 2020). Asthenospheric porosity in these models at a given snapshot in time can reach up to 10%–20%, which could explain our melt fraction observations in the channels (Sim et al., 2020). The melt may also reduce the asthenospheric viscosity (Hirth & Kohlstedt, 1995; Jackson et al., 2006) potentially further promoting small-scale convection.

Partial melt is inferred in different geometries beneath the two different ridge segments in our study region, including punctuated anomalous regions impinging on the base of the plate, channels of melt beneath the plate, and punctuated regions at deeper depth. Interestingly, the deeper melt exists at depths greater than predicted from simple adiabatic upwelling models and are completely disconnected from the shallower melts. The variable geometries may be related to the 3-D nature of the study area, and may also suggest that we are imaging different stages in melt generation and migration, rather than steady-state equilibrium melt. Our observations in light of these geodynamic models suggests that melt is dynamic but may be persistent on geological timescales.

5. Conclusions

We develop a simple relationship for shear velocity and resistivity of the oceanic lithosphere and asthenosphere that can be used to initialize these quantities for joint inversions based on data from the I-LAB experiments and petrophysical modeling. We use the relationship to create a shear-wave starting model that we used to re-invert the phase velocities. The new shear-wave velocity model more closely resembles the resistivity models, in particular by including a low-velocity channel and also in terms of the location and shape of slow velocity anomalies. The apparent lithospheric drip was also enhanced. Overall, the correlation between the surface wave and MT data sets is increased. This suggests that apparent discrepancies between the original models are more likely an artifact of resolution and inversion schemes. Surface waves cannot resolve thin channel structures unless prior knowledge is used in the starting model in the inversion. We also demonstrate the utility for shear velocity inversion guided by resistivity structure for mantle melting and thermal structure based on petrophysical modeling. We show that shear velocity can place good constraints on melt volume, while resistivity can place good constraints on melt water content, CO_2 content or the presence of sulfide melt given a simple thermal structure such as the half-space cooling model.

Our estimates of melt, melt water content, and temperature are in general reasonable and within the expectations given geochemical outputs from the nearby ridge segments. The one exception is very high water or CO_2 contents (>15%) estimated in the slowest and least resistive anomalies. These high melt water or CO_2 contents could be real but would require coalescing low degree partial melts of moderately wet or carbon-rich mantle sources. Alternatively, nearly pure sulfide melts at small fractions could potentially partially explain these anomalies. Overall, joint interpretation and/or inversion of resistivity and shear velocity models holds promise for resolving debates about the lithosphere-asthenosphere system and the presence and character of partial melt in the mantle.

Data Availability Statement

Seismic data are archived at the IRIS DMC, as 2016–2017 network XS https://doi.org/10.7914/SN/XS_2016 (Rychert et al., 2016).

Acknowledgments
C. A. Rychert, N. Harmon, and J. M. Kendall were funded by the Natural Environment Research Council (NE/M003507/1 and NE/M004643/1) and the European Research Council (GA 638665). S. Constable was funded by the National Science Foundation under Grant OCE-1536400 (CA-LAB). S. Wang was funded by the Seafloor Electromagnetic Methods Consortium at Scripps Institution of Oceanography and the Norwegian Research Council and the GAMES consortium at NTNU (grant 294404). The authors would also like to thank the Associate Editor Max Moorkamp and two anonymous reviewers for their constructive comments. The authors also thank the captains and crews of RV Langseth (MGL2016-02) and RRS Discovery (DY072) for their assistance with the data collection.

References

Abers, G. A., Fischer, K. M., Hirth, G., Wiens, D. A., Plank, T., Holtzman, B. K., et al. (2014). Reconciling mantle attenuation-temperature relationships from seismology, petrology, and laboratory measurements. *Geochemistry, Geophysics, Geosystems*, *15*(9), 3521–3542. https://doi.org/10.1002/2014gc005444

Abubakar, A., Gao, G., Habashy, T. M., & Liu, J. (2012). Joint inversion approaches for geophysical electromagnetic and elastic full-waveform data. *Inverse Problems*, *28*(5), 055016. https://doi.org/10.1088/0266-5611/28/5/055016

Agius, M., Harmon, N., Rychert, C. A., Tharimena, S., & Kendall, J. M. (2018). Sediment characterization at the Equatorial Mid-Atlantic Ridge from P-to-S teleseismic phase conversions recorded on the PI-LAB Experiment. *Geophysical Research Letters*, *45*, 12244–12252. https://doi.org/10.1029/2018GL080565

Agius, M. R., Rychert, C. A., Harmon, N., Tharimena, S., & Kendall, J.-M. (2021). A thin mantle transition zone beneath the equatorial Mid-Atlantic Ridge. *Nature*, *589*(7843), 562–566. http://doi.org/10.1038/s41586-020-03139-x

Anderson, D., & Sammis, C. (1970). Partial melting in the upper mantle. *Physics of the Earth and Planetary Interiors*, *3*, 41–50. https://doi.org/10.1016/0031-9201(70)90042-7

Baba, K., Chave, A. D., Evans, R. L., Hirth, G., & Mackie, R. L. (2006). Mantle dynamics beneath the East Pacific Rise at 17 degrees S: Insights from the Mantle Electromagnetic and Tomography (MELT) experiment. *Journal of Geophysical Research*, *111*(B02101). https://doi.org/10.1029/2004JB003598

Bell, S., Ruan, Y. Y., & Forsyth, D. W. (2016). Ridge asymmetry and deep aqueous alteration at the trench observed from Rayleigh wave tomography of the Juan de Fuca plate. *Journal of Geophysical Research: Solid Earth*, *121*(10), 7298–7321. https://doi.org/10.1002/2016jb012990

Bennington, N. L., Zhang, H. J., Thurber, C. H., & Bedrosian, P. A. (2015). Joint inversion of seismic and magnetotelluric data in the Parkfield Region of California using the normalized cross-gradient constraint. *Pure and Applied Geophysics*, *172*(5), 1033–1052. https://doi.org/10.1007/s00024-014-1002-9

Clark, A. N., & Lesher, C. E. (2017). Elastic properties of silicate melts: Implications for low velocity zones at the Lithosphere-Asthenosphere Boundary. *Science Advances*, *3*(12). https://doi.org/10.1126/sciadv.1701312

Colombo, D., & Rovetta, D. (2018). Coupling strategies in multiparameter geophysical joint inversion. *Geophysical Journal International*, *215*(2), 1171–1184. https://doi.org/10.1093/gji/ggy341

Dasgupta, R., & Hirschmann, M. M. (2010). The deep carbon cycle and melting in Earth's interior. *Earth and Planetary Science Letters*, *298*(1–2), 1–13. https://doi.org/10.1016/j.epsl.2010.06.039

Ducea, M. N., & Park, S. K. (2000). Enhanced mantle conductivity from sulfide minerals, Southern Sierra Nevada, California. *Geophysical Research Letters*, *27*(16), 2405–2408. https://doi.org/10.1029/2000GL011565

Dunn, R. A., & Forsyth, D. W. (2003). Imaging the transition between the region of mantle melt generation and the crustal magma chamber beneath the southern East Pacific Rise with short-period Love waves. *Journal of Geophysical Research*, *108*(B7), 2352. https://doi.org/10.1029/2002JB002217

Dziewonski, A. M., & Anderson, D. L. (1981). Preliminary Reference Earth Model. *Physics of the Earth and Planetary Interiors*, *25*(4), 297–356. https://doi.org/10.1016/0031-9201(81)90046-7

Evans, R. L., Tarits, P., Chave, A. D., White, A., Heinson, G., Filloux, J. H., et al. (1999). Asymmetric electrical structure in the mantle beneath the East Pacific Rise at 17 degrees S. *Science*, *286*(5440), 752–756. https://doi.org/10.1126/science.286.5440.752

Fischer, K. M., Rychert, C. A., Dalton, C. A., Miller, M. S., Beghein, C., & Schutt, D. L. (2020). A comparison of oceanic and continental mantle lithosphere. *Physics of the Earth and Planetary Interiors*, *309*, 106600. http://doi.org/10.1016/j.pepi.2020.106600

Forsyth, D. W., & Li, A. (2005). Array-analysis of two-dimensional variations in surface wave phase velocity and azimuthal anisotropy in the presence of multipathing interference. In A. Levander, & G. Nolet (Eds.), *Seismic data analysis and imaging with global and local arrays*. AGU Monograph. https://doi.org/10.1029/157gm06

Forsyth, D. W., Scheirer, D. S., Webb, S. C., Dorman, L. M., Orcutt, J. A., Harding, A. J., et al. (1998). Imaging the deep seismic structure beneath a Mid-Ocean Ridge: The MELT experiment. *Science*, *280*(5367), 1215–1218. https://doi.org/10.1126/science.280.5367.1235

Frost, B. R., Fyfe, W. S., Tazaki, K., & Chan, T. (1989). Grain-boundary graphite in rocks and implications for high electrical-conductivity in the lower crust. *Nature*, *340*(6229), 134–136. https://doi.org/10.1038/340134a0

Gaherty, J. B., Jordan, T. H., & Gee, L. S. (1996). Seismic structure of the upper mantle in a central Pacific corridor. *Journal of Geophysical Research*, *101*(B10), 22291–22309. https://doi.org/10.1029/96jb01882

Gallardo, L. A., & Meju, M. A. (2004). Joint two-dimensional DC resistivity and seismic travel time inversion with cross-gradients constraints. *Journal of Geophysical Research*, *109*(B3), B03311. https://doi.org/10.1029/2003jb002716

Gao, H. Y. (2016). Seismic velocity structure of the Juan de Fuca and Gorda plates revealed by a joint inversion of ambient noise and regional earthquakes. *Geophysical Research Letters*, *43*(10), 5194–5201. https://doi.org/10.1002/2016gl069381

Gardés, E., Gaillard, F., & Tarits, P. (2014). Toward a unified hydrous olivine electrical conductivity law. *Geochemistry, Geophysics, Geosystems*, *15*(12), 4984–5000. https://doi.org/10.1002/2014GC005496

Goetze, C., Poirier, J. P., Kelly, A., Cook, A. H., & Greenwood, G. W. (1978). The mechanisms of creep in olivine. *Philosophical Transactions of the Royal Society of London—Series A: Mathematical and Physical Sciences*, *288*(1350), 99–119. https://doi.org/10.1098/rsta.1978.0008

Guo, R., Yao, H. M., Li, M., Ng, M. K. P., Jiang, L., & Abubakar, A. (2020). Joint inversion of audio-magnetotelluric and seismic travel time data with deep learning constraint. *IEEE Transactions on Geoscience and Remote Sensing*, 1–14. https://doi.org/10.1109/TGRS.2020.3032743

Haber, E., & Oldenburg, D. (1997). Joint inversion: A structural approach. *Inverse Problems*, *13*(1), 63–77. https://doi.org/10.1088/0266-5611/13/1/006

Hacker, B. R., & Abers, G. A. (2004). Subduction factory 3: An Excel worksheet and macro for calculating the densities, seismic wave speeds, and H_2O contents of minerals and rocks at pressure and temperature. *Geochemistry, Geophysics, Geosystems*, *5*, Q01005. https://doi.org/10.1029/2003gc000614

Hammond, W. C., & Humphreys, E. D. (2000). Upper mantle seismic wave velocity: Effects of realistic partial melt geometries. *Journal of Geophysical Research*, *105*(5), 10975–10986. https://doi.org/10.1029/2000jb900041

Harmon, N., Rychert, C. A., Agius, M. R., Tharimena, S., Le Bas, T. P., Kendall, J. M., & Constable, S. (2018). Marine geophysical investigation of the Chain Fracture Zone in the equatorial Atlantic from the PI-LAB Experiment. *Journal of Geophysical Research: Solid Earth*, *123*, 11016–11030. https://doi.org/10.1029/2018JB015982

Harmon, N., Rychert, C. A., Kendall, J., Tharimena, S., Bogiatzis, P., & Agius, M. (2020). Evolution of the oceanic Lithosphere in the equatorial Atlantic from Rayleigh Wave tomography, evidence for small-scale convection from the PI-LAB experiment. *Geochemistry, Geophysics, Geosystems*, *21*. https://doi.org/10.1029/2020GC009174

Havlin, C., Holtzman, B., & Hopper, E. (2021). Inference of thermodynamic state in the asthenosphere from anelastic properties, with applications to North American upper mantle. *Physics of the Earth and Planetary Interiors*, *314*, 106639. https://doi.org/10.1016/j.pepi.2020.106639

Helffrich, G., Kendall, J.-M., Hammond, J. O. S., & Carroll, M. R. (2011). Sulfide melts and long-term low seismic wavespeeds in lithospheric and asthenospheric mantle. *Geophysical Research Letters*, *38*(11). https://doi.org/10.1029/2011GL047126

Herrmann, R. B. (2013). Computer programs in seismology: An evolving tool for instruction and research. *Seismological Research Letters*, *84*(6), 1081–1088. https://doi.org/10.1785/0220110096

Hicks, S. P., Okuwaki, R., Steinberg, A., Rychert, C. A., Harmon, N., Abercrombie, R. E., et al. (2020). Back-propagating supershear rupture in the 2016 Mw 7.1 Romanche transform fault earthquake. *Nature Geoscience*, *13*(9), 647–653. https://doi.org/10.1038/s41561-020-0619-9

Hirschmann, M. M. (2010). Partial melt in the oceanic low velocity zone. *Physics of the Earth and Planetary Interiors*, *179*(1–2), 60–71. https://doi.org/10.1016/J.Pepi.2009.12.003

Hirth, G., & Kohlstedt, D. L. (1995). Experimental Constraints on the dynamics of the partially molten upper-mantle.2. Deformation in the Dislocation Creep Regime. *Journal of Geophysical Research*, *100*(8), 15441–15449. https://doi.org/10.1029/95jb01292

Jackson, I., & Faul, U. H. (2010). Grainsize-sensitive viscoelastic relaxation in olivine: Towards a robust laboratory-based model for seismological application. *Physics of the Earth and Planetary Interiors*, *183*(1–2), 151–163. https://doi.org/10.1016/J.Pepi.2010.09.005

Jackson, I., Faul, U. H., Fitz Gerald, J. D., & Morris, S. J. S. (2006). Contrasting viscoelastic behavior of melt-free and melt-bearing olivine: Implications for the nature of grain-boundary sliding. *Materials Science and Engineering: A—Structural Materials Properties Microstructure and Processing*, *442*(1–2), 170–174. https://doi.org/10.1016/J.Msea.2006.01.136

Jegen, M. D., Hobbs, R. W., Tarits, P., & Chave, A. (2009). Joint inversion of marine magnetotelluric and gravity data incorporating seismic constraints: Preliminary results of sub-basalt imaging off the Faroe Shelf. *Earth and Planetary Science Letters*, *282*(1), 47–55. https://doi.org/10.1016/j.epsl.2009.02.018

Johansen, S. E., Panzner, M., Mittet, R., Amundsen, H. E. F., Lim, A., Vik, E., et al. (2019). Deep electrical imaging of the ultraslow-spreading Mohns Ridge. *Nature*, *567*(7748), 379–383. https://doi.org/10.1038/s41586-019-1010-0

Karato, S.-I. (2012). On the origin of the asthenosphere. *Earth and Planetary Science Letters*, *321–322*, 95–103. https://doi.org/10.1016/j.epsl.2012.01.001

Katz, R. F., Spiegelman, M., & Langmuir, C. H. (2003). A new parameterization of hydrous mantle melting. *Geochemistry, Geophysics, Geosystems*, *4*(9), 1073. https://doi.org/10.1029/2002GC000433

Kawakatsu, H., Kumar, P., Takei, Y., Shinohara, M., Kanazawa, T., Araki, E., & Suyehiro, K. (2009). Seismic evidence for sharp Lithosphere-Asthenosphere Boundaries of oceanic plates. *Science*, *324*(5926), 499–502. https://doi.org/10.1126/science.1169499

Key, K. (2016). MARE2DEM: A 2-D inversion code for controlled-source electromagnetic and magnetotelluric data. *Geophysical Journal International*, *207*(1), 571–588. https://doi.org/10.1093/gji/ggw290

Key, K., Constable, S., Liu, L., & Pommier, A. (2013). Electical image of passive mantel upwelling beneath the northern East Pacific Rise. *Nature*, *495*, 499–502. https://doi.org/10.1038/nature11932

Le Voyer, M., Cottrell, E., Kelley, K. A., Brounce, M., & Hauri, E. H. (2015). The effect of primary versus secondary processes on the volatile content of MORB glasses: An example from the equatorial Mid-Atlantic Ridge (5 degrees N-3 degrees S). *Journal of Geophysical Research: Solid Earth*, *120*(1), 125–144. https://doi.org/10.1002/2014jb011160

Le Voyer, M., Hauri, E. H., Cottrell, E., Kelley, K. A., Salters, V. J. M., Langmuir, C. H., et al. (2019). Carbon Fluxes and primary magma CO_2 Contents along the global Mid-Ocean Ridge System. *Geochemistry, Geophysics, Geosystems*, *20*(3), 1387–1424. https://doi.org/10.1029/2018GC007630

McKenzie, D., & Parker, R. (1967). The North Pacific: An Example of Tectonics on a Sphere. *Nature*, *216*, 1276–1280. https://doi.org/10.1038/2161276a0

Mehouachi, F., & Singh, S. (2018). Water-rich sublithospheric melt channel in the equatorial Atlantic Ocean. *Nature Geoscience*, *11*, 65–69. https://doi.org/10.1038/s41561-017-0034-z

Moorkamp, M., Heincke, B., Jegen, M., Roberts, A. W., & Hobbs, R. W. (2011). A framework for 3-D joint inversion of MT, gravity and seismic refraction data. *Geophysical Journal International*, *184*(1), 477–493. https://doi.org/10.1111/j.1365-246X.2010.04856.x

Moorkamp, M., Jones, A. G., & Fishwick, S. (2010). Joint inversion of receiver functions, surface wave dispersion, and magnetotelluric data. *Journal of Geophysical Research*, *115*, B04318. https://doi.org/10.1029/2009jb006369

Naif, S., Key, K., Constable, S., & Evans, R. L. (2013). Melt-rich channel observed at the lithosphere-asthenosphere boundary. *Nature*, *495*(7441), 356–359. https://doi.org/10.1038/nature11939

Naif, S., Selway, K., Murphy, B. S., Egbert, G., & Pommier, A. (2021). Electrical conductivity of the lithosphere-asthenosphere system. *Physics of the Earth and Planetary Interiors*, *313*, 106661. https://doi.org/10.1016/j.pepi.2021.106661

Ni, H., Keppler, H., & Behrens, H. (2011). Electrical conductivity of hydrous basaltic melts: Implications for partial melting in the upper mantle. *Contributions to Mineralogy and Petrology*, *162*(3), 637–650. https://doi.org/10.1007/s00410-011-0617-4

Parker, R. L., & Oldenburg, D. W. (1973). Thermal Model of ocean ridges. *Nature; Physical Science*, *242*(122), 137–139. https://doi.org/10.1038/physci242137a0

Priestley, K., & McKenzie, D. (2006). The thermal structure of the lithosphere from shear wave velocities. *Earth and Planetary Science Letters*, *244*(1–2), 285–301. https://doi.org/10.1016/j.epsl.2006.01.008

Rychert, C. A., Fischer, K. M., & Rondenay, S. (2005). A sharp lithosphere-asthenosphere boundary imaged beneath eastern North America. *Nature*, *436*(7050), 542–545. https://doi.org/10.1038/nature03904

Rychert, C. A., & Harmon, N. (2017). Constraints on the anisotropic contributions to velocity discontinuities at ~60 km depth beneath the Pacific. *Geochemistry, Geophysics, Geosystems*, *18*, 2855–2871. https://doi.org/10.1002/2017GC006850

Rychert, C. A., & Harmon, N. (2018). Predictions and Observations for the Oceanic Lithosphere From S-to-P Receiver Functions and SS Precursors. *Geophysical Research Letters*, *45*(11), 5398–5406. http://doi.org/10.1029/2018gl077675

Rychert, C. A., Harmon, N., Constable, S., & Wang, S. G. (2020). The nature of the Lithosphere-Asthenosphere Boundary. *Journal of Geophysical Research: Solid Earth*, *125*(10), e2018JB016463. https://doi.org/10.1029/2018JB016463
Rychert, C. A., Harmon, N., & Tharimena, S. (2018a). Scattered wave imaging of the oceanic plate in Cascadia. *Science Advances*, *4*(2), eaao1908. http://doi.org/10.1126/sciadv.aao1908
Rychert, C. A., Harmon, N., & Tharimena, S. (2018b). Seismic imaging of the base of the ocean plates. In H. Yuan (Ed.), *Lithospheric discontinuities* (pp. 71–87). AGU Monographs. https://doi.org/10.1002/9781119249740.ch4
Rychert, C. A., Kendall, J. M., & Harmon, N. (2016). *Passive imaging of the lithosphere-asthenosphere boundary*.
Rychert, C. A., Rondenay, S., & Fischer, K. M. (2007). P-to-S and S-to-P imaging of a sharp Lithosphere-Asthenosphere Boundary beneath eastern North America. *Journal of Geophysical Research*, *112*(B8), B08314. https://doi.org/10.1029/2006jb004619
Rychert, C. A., & Shearer, P. M. (2009). A global view of the Lithosphere-Asthenosphere Boundary. *Science*, *324*(5926), 495–498. https://doi.org/10.1126/Science.1169754
Rychert, C. A., & Shearer, P. M. (2011). Imaging the Lithosphere-Asthenosphere Boundary beneath the Pacific using SS waveform modeling. *Journal of Geophysical Research*, *116*(7), B07307. https://doi.org/10.1029/2010jb008070
Rychert, C. A., Tharimena, S., Harmon, N., Wang, S., Constable, S., Kendall, J. M., et al. (2021). A dynamic lithosphere-asthenosphere boundary near the equatorial Mid-Atlantic Ridge. *Earth and Planetary Science Letters*, *566*, 116949. https://doi.org/10.1016/j.epsl.2021.116949
Saikia, U., Rychert, C., Harmon, N., & Kendall, J. M. (2020). Sediment structure at the equatorial mid-atlantic ridge constrained by seafloor admittance using data from the PI-LAB experiment. *Marine Geophysical Research*, *41*(1). http://doi.org/10.1007/s11001-020-09402-0
Saikia, U., Rychert, C., Harmon, N., & Kendall, J. M. (2021). Upper mantle anisotropic shear velocity structure at the Equatorial Mid-Atlantic Ridge constrained by Rayleigh Wave ch7lm the PI-LAB Experiment. *Geochemistry, Geophysics, Geosystems*, *22*(3), e2020GC009495. https://doi.org/10.1029/2020GC009495
Schmeling, H. (1985). Numerical-models on the influence of partial melt on elastic, anelastic and electric properties of rocks.1. Elasticity and anelasticity. *Physics of the Earth and Planetary Interiors*, *41*(1), 34–57. https://doi.org/10.1016/0031-9201(85)90100-1
Schmerr, N. (2012). The Gutenberg Discontinuity: Melt at the Lithosphere-Asthenosphere Boundary. *Science*, *335*(6075), 1480–1483. https://doi.org/10.1126/science.1215433
Schutt, D. L., & Lesher, C. E. (2006). Effects of melt depletion on the density and seismic velocity of garnet and spinel lherzolite. *Journal of Geophysical Research*, *111*(B5), B05401. https://doi.org/10.1029/2003JB002950
Seton, M., Müller, R. D., Zahirovic, S., Williams, S., Wright, N. M., Cannon, J., et al. (2020). A global data set of present-day oceanic crustal age and seafloor spreading parameters. *Geochemistry, Geophysics, Geosystems*, *21*(10), e2020GC009214. https://doi.org/10.1029/2020GC009214
Sifre, D., Gardes, E., Massuyeau, M., Hashim, L., Hier-Majumder, S., & Gaillard, F. (2014). Electrical conductivity during incipient melting in the oceanic low-velocity zone. *Nature*, *509*(7498), 81–85. https://doi.org/10.1038/nature13245
Sim, S. J., Spiegelman, M., Stegman, D. R., & Wilson, C. (2020). The influence of spreading rate and permeability on melt focusing beneath mid-ocean ridges. *Physics of the Earth and Planetary Interiors*, *304*, 106486. https://doi.org/10.1016/j.pepi.2020.106486
Smith, W. H. F., & Sandwell, D. T. (1997). Global seafloor topography from satellite altimetry and ship soundings. *Science*, *277*, 1957–1962. https://doi.org/10.1126/science.277.5334.1956
Spiegelman, M., & Elliott, T. (1993). Consequences of melt transport for uranium series disequilibrium in young lavas. *Earth and Planetary Science Letters*, *118*(1), 1–20. https://doi.org/10.1016/0012-821X(93)90155-3
Stern, T. A., Henrys, S. A., Okaya, D., Louie, J. N., Savage, M. K., Lamb, S., et al. (2015). A seismic reflection image for the base of a tectonic plate. *Nature*, *518*(7537), 85–88. https://doi.org/10.1038/nature14146
Stesky, R. M., & Brace, W. F. (1973). Electrical conductivity of serpentinized rocks to 6 kilobars. *Journal of Geophysical Research*, *78*(32), 7614–7621. https://doi.org/10.1029/JB078i032p07614
Stixrude, L., & Lithgow-Bertelloni, C. (2005). Mineralogy and elasticity of the oceanic upper mantle: Origin of the low-velocity zone. *Journal of Geophysical Research*, *110*, B03204. https://doi.org/10.1029/2004jb002965
Sun, J., & Li, Y. (2016). Joint inversion of multiple geophysical and petrophysical data using generalized fuzzy clustering algorithms. *Geophysical Journal International*, *208*(2), 1201–1216. https://doi.org/10.1093/gji/ggw442
Takei, Y. (1998). Constitutive mechanical relations of solid-liquid composites in terms of grain-boundary contiguity. *Journal of Geophysical Research*, *103*(B8), 18183–18203. https://doi.org/10.1029/98JB01489
Takougang, E. M. T., Harris, B., Kepic, A., & Le, C. V. A. (2015). Cooperative joint inversion of 3D seismic and magnetotelluric data: With application in a mineral province. *Geophysics*, *80*(4), R175–R187. https://doi.org/10.1190/geo2014-0252.1
Tan, Y., & Helmberger, D. V. (2007). Trans-Pacific upper mantle shear velocity structure. *Journal of Geophysical Research*, *112*(8), B08301. https://doi.org/10.1029/2006jb004853
Tharimena, S., Rychert, C., Harmon, N., & White, P. (2017). Imaging Pacific lithosphere seismic discontinuities—Insights from SS precursor modeling. *Journal of Geophysical Research: Solid Earth*, *122*(3), 2131–2152. https://doi.org/10.1002/2016jb013526
Turcotte, D., & Schubert, G. (2002). *Geodynamics* (2nd ed.). Cambridge University Press.
Wang, S. G., Constable, S., Reyes-Ortega, V., Jahandari, H., Farquharson, C., & Esquivel, T. A. (2021). Two-dimensional determinant inversion of marine magnetotelluric data and a field example from the Gulf of California, Mexico. *Geophysics*, *86*(1), E37–E57. https://doi.org/10.1190/geo2019-0735.1
Wang, S. G., Constable, S., Reyes-Ortega, V., & Rychert, C. A. (2019). A newly distinguished marine magnetotelluric coast effect sensitive to the lithosphere-asthenosphere boundary. *Geophysical Journal International*, *218*(2), 978–987. https://doi.org/10.1093/gji/ggz202
Wang, S. G., Constable, S., Rychert, C. A., & Harmon, N. (2020). A Lithosphere-Asthenosphere Boundary and partial melt estimated using marine magnetotelluric data at the Central Middle Atlantic Ridge. *Geochemistry, Geophysics, Geosystems*, *21*(9), e2020GC009177. https://doi.org/10.1029/2020GC009177
Workman, R. K., & Hart, S. R. (2005). Major and trace element composition of the depleted MORB mantle (DMM). *Earth and Planetary Science Letters*, *231*(1–2), 53–72. https://doi.org/10.1016/j.epsl.2004.12.005
Yamauchi, H., & Takei, Y. (2016). Polycrystal anelasticity at near-solidus temperatures. *Journal of Geophysical Research: Solid Earth*, *121*(11), 7790–7820. https://doi.org/10.1002/2016jb013316
Zhang, R., Li, T., Deng, X., Huang, X., & Pak, Y. (2020). Two-dimensional data-space joint inversion of magnetotelluric, gravity, magnetic and seismic data with cross-gradient constraints. *Geophysical Prospecting*, *68*(2), 721–731. https://doi.org/10.1111/1365-2478.12858